UNIVERSITY
OF LATVIA

Department of Physics, Mathematics and Optometry
University of Latvia

# THREE-DIMENSIONAL SIMULATIONS OF MAGNETIC FLUID FREE INTERFACE DYNAMICS USING BOUNDARY INTEGRAL EQUATIONS

**Aigars Langins**

This dissertation is submitted for the degree of
*Doctor of Physics*

Scientific advisor:
Dr. habil. phys. Andrejs Cēbers

Riga, 2022

# Acknowledgements

This dissertation would not have been possible without many people to whom I am profoundly thankful.

First of all, I want to dedicate my deepest gratitude to my thesis advisor Prof. Andrejs Cēbers who has guided me through countless obstacles and seeming dead-ends, always leaving me excited and enlightened after our many discussions. After some years, I will probably have forgotten many of the equations and methods encountered in this thesis, but I will never forget his wisdom about proceeding through difficulties:

“*If you don't know what to do, do something.*”

Next, a huge thanks goes to my brother-in-arms Andris P. Stikuts, whose assistance spanned many dimensions from helping with writing the code and providing experimental data to discussing physics and reigniting my curiosity during times of lower morale.

I also want to thank my friends and family for the endless encouragement they never failed to share with me. A particular gratitude goes to my great wife Zane Jansone-Langina whose support in terms of countless dinners, reminders to have enough sleep and motivational nudges ensured my health and spirits are always high enough.

Finally, I wish to thank the European Union's H2020-MSCA-ITN project “Magnetics and Microfluidics (MAMI)” (grant no. 766007) for the financial support, and the many training experiences and the numerous new friendships it has provided.

Aigars Langins

# Abstract

This dissertation tackles the problem of describing the complex phenomena magnetic fluid droplets undergo under certain external magnetic field configurations, which has proven to be elusive of a quantitative description, except in the simplest of cases. To address this problem, a mathematical model of the full three-dimensional free surface dynamics of magnetic fluid droplets in magnetic fields is required. A particular model relying on solving boundary integral equations, as well as its algorithmic implementation is presented in this work. The algorithm can handle arbitrary droplet and carrier fluid viscosity ratios and can capture various shape instabilities the droplet might undergo under the right magnetic field conditions, like sharp conical tip development or transforming into a starfish-like form. It enables the evaluation of various approximations often used to describe ellipsoidal droplets, by comparing the droplet dynamics calculated from such approximations to the results achieved from first principles with this numerical tool. The algorithm may also be used to explore droplet configurations in arbitrary magnetic fields, as well as to indirectly calculate the physical properties of magnetic fluid droplets and to predict the magnetic field thresholds above which the droplet shape can develop surface instabilities.

Keywords: Stokes Flow, Boundary Integral, Magnetic Fluid, Instability, Equilibrium Figures.

# Anotācija

Šī disertācija aplūko problēmu par magnētiska šķidruma piliena sarežģīto uzvedību ārēju magnētisko lauku ietekmē, kas līdz šim ir bijusi kvantitatīvi risināma tikai vienkāršākajos gadījumos. Problēmas risināšanai ir nepieciešams matemātisks modelis, kas apraksta pilnu magnētiska šķidruma piliena brīvās virsmas dinamiku ārējos magnētiskos laukos trijās dimensijās. Disertācijā prezentēts konkrēts modelis, kas balstās uz robežintegrālvienādojumu risināšanu, kā arī tā algoritmiskā implementācija. Algoritms var veikt aprēķinus ar patvaļīgām piliena un apkārtesošā šķidruma viskozitātēm, kā arī modelēt dažādas piliena virsmas nestabilitātes, kuras var izpausties īpašos magnētiskā lauka apstākļos, piemēram, konisku asumu rašanos vai transformēšanos jūraszvaigznei līdzīgā formā. Tas ļauj testēt dažādu pilienu aprakstā izmantotu aproksimāciju pielietojamības robežas, salīdzinot to paredzētos rezultātus ar skaitliskajiem rezultātiem, kas iegūti no pirmajiem principiem. Skaitlisko rīku var izmantot, lai pētītu magnētisku pilienu konfigurācijas patvaļīgos magnētiskos laukos, netieši noteiktu to fizikālos parametrus un īpašības un atrastu kritiskos magnētiskos laukus, kādi ir nepieciešami dažādo virsmas nestabilitāšu novērošanai.

Atslēgvārdi: Stoksa plūsma, Robežintegrāļi, Magnētiski šķidrumi, Nestabilitātes, Līdzsvara figūras.

# Contents

# List of Figures

# Chapter 1

# Introduction

## Contents

## 1.1 General motivation

At microscopic length scales fluid systems often behave differently than we might have grown accustomed to at our everyday dimensions. It is because at these small lengths the fluid dynamics is mostly governed by the interfacial effects, that scale with the square of the length, rather than the bulk effects that scale with the third power. Introducing magnetic effects at these small scales, of course, makes these systems even more complicated. A particularly complex and nonlinear behaviour can be observed at the boundary between immiscible fluids, for example, if we consider a magnetic fluid droplet suspended in a non-magnetic carrier liquid, where the equilibriation of magnetic energy and surface tension might create unimaginably intricate labyrinthine structures or develop instabilities of sharp interfaces, as well as synchronized group dynamics of particles.

It is difficult to describe the highly nonlinear world of magnetic fluid droplets analytically, so scientists must also rely on numerical tools in their exploration. Sometimes numerical approaches can prove to be a more detailed method of investigation, as they are able to quantify otherwise difficult to measure quantities, for example stresses or pressure fields inside the fluids. Numerical tools also allow to explore specific physical effects with a great degree of accuracy of the relevant parameter values.

The author finds the idea of trying to capture even a small part of the aforementioned astonishing phenomena inspiring and so has dedicated his dissertation to the subject of numerical investigation of magnetic fluid droplets.

## 1.2 Recent developments in the field

Mathematical physics has long been concerned with equilibrium figures various objects might assume in different external physical conditions. For example, the classical problem of self-gravitating masses [1] allowed for the exploration of many bifurcations of surface shapes. The seminal paper by G.I.Taylor [2] sparked vast research into the the equilibrium shapes an electrically or magnetically responsive fluid might take, as well as their dynamics under the action of external electromagnetic fields. In particular, significant breakthrough in the research of droplets under the action of electromagnetic field arose with the synthesis of magnetic liquids [3] allowing many interesting effects to be observed and described, such as the droplet deformation and its dynamics under the action of static magnetic fields [4, 5, 6], rotating fields [7, 8] and labyrinthine pattern formation in the Hele-Shaw cells [9, 10] or of systems of vanishing interfacial tension [11]. For the description of these effects different approximate methods [12, 13, 14] (assumption of ellipsoidal shape, satisfaction of boundary conditions on average and others) were created which need to be confirmed. Even more different observed phenomena still are not described theoretically or sufficiently explored numerically, – such as the dynamics of hysteresis of droplet deformation [15], re-entrant transition of figures of equilibrium of magnetic droplets in a high frequency rotating field [7], spike formation on the droplet's poles [16] and others. It should be noted that droplets under the action of electromagnetic field have many uses such as investigation of mechanical properties of tissue [17], dynamic self assembly [16], magnetohydrodynamic induction pumps [18], microfluidics [19, 20], junction sealing [21], magnetic hyperthermia for cancer therapy [22], microrobotics for cargo transportation [23, 24], programmable droplets for flow control [25] and many others.

In parallel with the experimental investigation of magnetic droplets, significant efforts in the development of the numerical methods for their simulation have been undertaken. Efficient tools for the simulation of the free boundary phenomena may be developed on the basis of the boundary integral equations [26, 27]; they have recently been used to observe various "starfish" like droplet shape instabilities in a two-dimensional Hele-Shaw cell model [28]. In axisymmetric case these methods were developed in [29, 30]. Among the phenomena predicted is, for example, the formation of the spikes on the droplet's poles if the magnetic permeability is high enough [30, 31, 32]. It may be noted that by using boundary integral equation technique the simulation of such complicated free boundary problem as the formation of the labyrinthine patterns in the Hele-Shaw cells has been carried out [33]. The application of the boundary integral equation algorithm for the real three dimensional case is a real challenge since special care should be applied to keep the quality of mesh on the the droplets surface [34, 35, 36]. Modelling such dynamics can also be approached via the level-set method [37], the immersed boundary method [38] which is sensitive to precise boundary description[39] or Lattice Boltzmann methods which can handle complex fluid configurations and the coexistence of multiple fluid phases well [40]. A further review of magnetic fluid modelling and simulations is also available [41]. In parallel to the development of the numerical tools for the simulation of magnetic droplets, corresponding elaborations are taking place for simulation of droplets in leaky dielectrics where besides the usual terms, the convective surface charge transfer by the liquid motion should be taken into account [42].

One of the first undertakings to simulate magnetic droplets in the three dimensional case was undertaken in [43] under the condition of equal viscosities of the droplet and surrounding fluid. Since the viscosities of the concentrated phase of strongly magnetic droplets obtained by the demixing of magnetic colloids are significantly larger than the viscosity of the carrier liquid (usually water) [44] it is crucial in the simulation of their dynamics to account for that in the numerical models.

At present there do not exist exact solutions of magnetic droplet behaviour under the simultaneous action of viscous, magnetic and capillary forces which may be used as benchmarks for validating numerical models. In this situation the validations of the numerical models is carried out by the comparison of the numerical results with some approximate solutions. It is our aim here to carry out these comparisons using the simple model of a magnetic fluid droplet [3] using an extension of the numerical algorithm of [43].

## 1.3 Numerical Simulation Methods for Fluid Droplets

Magnetic fluid droplets can be investigated with optical methods, owing to their large enough dimensions, but such approaches are not as viable to measure, for example, the pressure or stress fields inside or around the droplet. In such cases numerical methods can be of great help by solving mathematical models of the underlying physical phenomena and comparing their results to experimental observations.

A review of common approaches to fluid droplets simulation are given in [45]. One of the most popular methods of fluid dynamics simulations is the Finite Element method (FEM), that solves the governing equations in cells of a volumetric mesh of the problem domain [46]. This approach often calls for a re-meshing in order to more accurately track the evolving interfaces. A different group of algorithms is the so called interface tracking methods, an example of which is the Volume of Fluid (VOF) [47]. It allows for comparatively easy tracking of fluid interfaces and drop coalescence or breakup, by assigning an occupancy fraction value to every mesh cell that indicates whether a fluid is present in that particular cell. VOF does not require regular re-meshing, as opposed to the FEM approach.

The methods outlined above posses a certain drawback regarding the simulation of magnetic fluid droplets, as they require a very fine mesh resolution to accurately describe the intricacies of the droplet surfaces which may take on rather complex shapes [7]. These mesh resolutions may be prohibitively expensive to obtain.

Another approach consists of the so called mesh-free methods, a popular example of which is the Boundary Element method (BEM) [48]. These methods are able to map the flow equations of the volume on to interfaces and surfaces of the problem domain [27]. Such a mapping effectively reduces the dimensionality of the problem from a three-dimensional interpretation throughout the whole domain, to a two-dimensional problem on the interfaces.

Further, integral equations allow to take into account various boundary conditions on these interfaces and provide a tool to relate the physical parameters like pressure, velocity, and stresses at a certain point on a particular boundary to those of all the other points on all boundaries. These boundary integral equations can be recast in the form of a linear system of equations for the relevant physical quantities.

As in BEM only the interfaces are discretized, this method typically leads to a relatively small degree of freedom of the meshes, whilst describing the relevant interface shape intricacies accurately. However, this dimensionality reduction from a bulk problem to a surface problem comes at the cost of dense linear systems, as every point of the mesh has to be considered in relation to every other point of the mesh. This method also requires particular care and re-meshing to describe topological changes of the droplet configuration, for example droplet coalescence or droplet breakup [36].

In this thesis we investigate the Boundary Element method, as we are particularly interested in the droplet interface dynamics and instabilities.

## 1.4 Magnetic Fluids

Having established the relevance and wide applications of magnetic fluids, we can dive into what they actually are. They have been first synthesized in the USA in the 1960s [49], and they fundamentally are fluids that are responsive to magnetic forces [50], for example, a magnetic fluid would climb the walls of a container, if a strong enough magnet was placed on the side of the container.

Magnetic fluids are an organization of a liquid medium intertwined with tiny solid, permanently magnetic particles, which are typically coated with a surfactant layer to prevent coagulation [3, 51], for example, consisting of citrate ions [52]. Further details about the synthesis and characterization of magnetic fluids can be found in [53, 54].

An example of such a system is a water based colloid with magnetic particles of nanometer size, also often referred to as a ferrofluid. Ferrofluids usually do not settle out at room conditions due to Brownian motion.

The object and interest of this work, microscopic magnetic fluid droplets can be obtained from forcing a water-based ferrofluid to demix into two phases – droplets with a large concentration of magnetic particles and a carrier fluid with a negligible magnetic particle concentration – by adding salt to the original colloid [52, 44]. Magnetic fluid droplets obtained in such way are said to be phase-separated. This method allows for production of droplets with sizes at the scale of microns and with particularly high magnetic susceptibilities.

## 1.5 Main objectives of this work

Since the simulation of magnetic fluid droplets in three dimensions is still a very nascent field, especially in the case of arbitrary droplet and carrier fluid viscosity ratios, the aim of this thesis is to develop a numerical simulation tool and with it an understanding of their behaviour in various magnetic fields.

In order to pursue this objective, the following problems are tackled:

- Develop a three-dimensional numerical algorithm for calculation of magnetic field and velocity field of fluids based on the boundary element method relying on boundary integral equations.
- Validate the developed algorithm with known theoretical relationships.
- Use the algorithm to probe the limits of various approximations, often used in this setting, e.g. the assumption of the elliptical form of the droplet.

- With the help of the algorithm, numerically explore full three-dimensional dynamics of magnetic fluid droplets in various field configurations.
- Numerically analyze droplet shape instability onsets and evolution, e.g. the "starfish" instability.
- Apply the algorithm to indirectly simultaneously obtain physical properties (surface tension, magnetic permeability and viscosity) of magnetic fluid droplets by fitting simulation results to experimental data.
- Numerically observe previously unseen effects, for example the back-and-forth motion of magnetic liquid droplet in a rotating magnetic field.

## 1.6 Outline of thesis

This thesis is organized in the following way. A general overview and recent developments of the field are given in the Chapter 1. Then, Chapter 2 introduces the relevant theoretical foundation of hydrodynamics and magnetostatics, and formulates the mathematical model of the physical problem. Next, Chapter 3 introduces the numerical algorithm and its intricacies, which is then validated with various known theoretical relationships, as explained in Chapter 4. Finally, simulations of magnetic fluid droplet behavior in various situations by the developed algorithm are explored in Chapter 5, concluding with a discussion and summarizing the main theses of this dissertation in Chapter 6.

# Chapter 2

# Mathematical model

## Contents

This chapter introduces the relevant mathematics and physical models that govern the microscopic magnetic fluid droplet dynamics. We first introduce the hydrodynamical problem and the solutions of it in terms of boundary integral equations. Then we introduce the magnetostatic problem and finally tie these topics together to arrive the equations of motion of a magnetic droplet.

## 2.1 Equations governing the hydrodynamics

Magnetic fluid droplets that we have concerned ourselves with here, typically reside in the microscopic domain, are assumed to be incompressible and to behave in Newtonian way, as well as flowing very slowly. Such assumptions allow the fluid to be described by the Stokes equations for incompressible fluids [27]:

$$-\boldsymbol{\nabla} p + \eta \Delta \boldsymbol{v} + \rho \boldsymbol{b} = \boldsymbol{0}, \qquad \boldsymbol{\nabla} \cdot \boldsymbol{v} = 0, \tag{2.1}$$

where $p$ is the pressure, $\eta$ is the dynamic viscosity, $\boldsymbol{v}$ is the velocity, $\rho$ is the density and $\boldsymbol{b}$ describes mass density of a body force.

### 2.1.1 Fundamental solution of Stokes equations

Considering an arbitrary point force $\boldsymbol{g}$ acting at a point $\boldsymbol{y}$, the Stokes equations become

$$-\boldsymbol{\nabla} p + \eta \Delta \boldsymbol{v} + \boldsymbol{g} \delta(\boldsymbol{x} - \boldsymbol{y}) = \boldsymbol{0}, \tag{2.2}$$

with $\delta$ representing the three-dimensional Dirac delta function. Here the differentiation is made with respect to the $\boldsymbol{x}$ variable. In such a case the pressure $p$, flow field $\boldsymbol{v}$ and the stress tensor at the point of observation $\boldsymbol{x}$ is given by [27]:

$$p(\boldsymbol{x}) = \frac{1}{8\pi} p_j(\boldsymbol{x}, \boldsymbol{y}) g_j, \tag{2.3}$$

$$v_i(\boldsymbol{x}) = \frac{1}{8\pi\eta} G_{ij}(\boldsymbol{x}, \boldsymbol{y}) g_j, \tag{2.4}$$

$$\sigma_{ik}(\boldsymbol{x}) = \frac{1}{8\pi} T_{ijk}(\boldsymbol{x}, \boldsymbol{y}) g_j, \tag{2.5}$$

where the flow field $\boldsymbol{v}$ is called the *fundamental solution* of the 3D Stokes equation. The fundamental solution and its corresponding pressure field is shown in Figure 2.1.

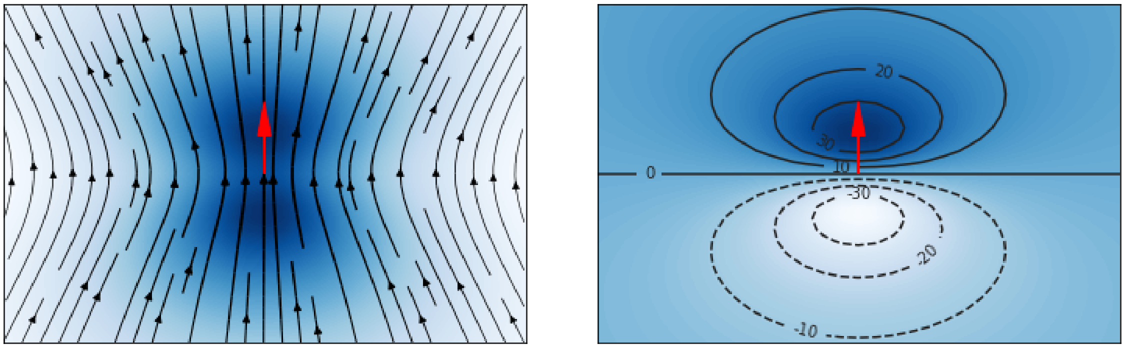

(a) Velocity field. The shading in background shows the magnitude of the velocity.

(b) Pressure field around the point force. The lines are contours of equivalent pressure values in arbitrary units.

Figure 2.1: Solutions to the Stokes equation with a point force $\boldsymbol{g}$, indicated by the red arrow.

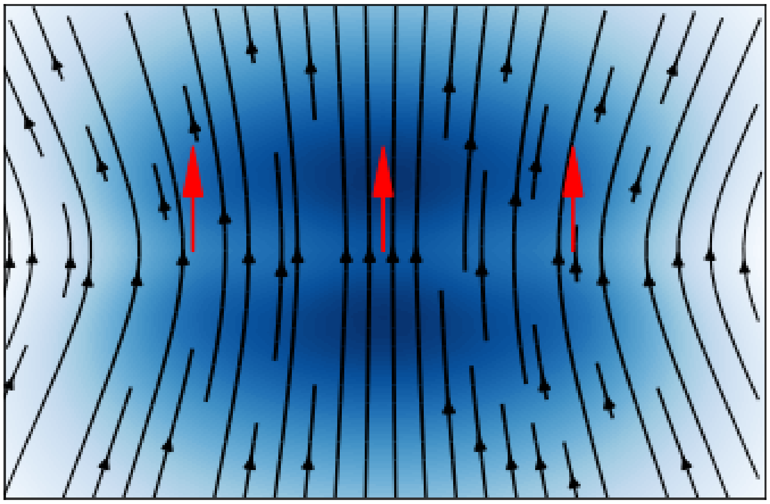

Figure 2.2: Linearity of the Stokes equation allows us to construct an arbitrary force distribution using a number of point forces (indicated by the red arrows). The shading in background shows the magnitude of the velocity.

The solutions contain the so-called *stokeslet*, that describes the linear relation between a point force $\boldsymbol{g}$ and the velocity $\boldsymbol{v}$, given by

$$G_{ik}(\boldsymbol{x},\boldsymbol{y}) = \frac{\delta_{ij}}{|\boldsymbol{x}-\boldsymbol{y}|} + \frac{(x_i - y_i)(x_j - y_j)}{|\boldsymbol{x}-\boldsymbol{y}|^3}, \tag{2.6}$$

the so-called *pressurelet*, relating the point force to pressure, given by

$$p_i(\boldsymbol{x},\boldsymbol{y}) = 2\frac{(x_i - y_i)}{|\boldsymbol{x}-\boldsymbol{y}|^3} \tag{2.7}$$

and the so-called *stresslet*, relating the point force and the stress tensor, given by

$$T_{ijk}(\boldsymbol{x},\boldsymbol{y}) = -6\frac{(x_i - y_i)(x_j - y_j)(x_k - y_k)}{|\boldsymbol{x}-\boldsymbol{y}|^5}. \tag{2.8}$$

In further equations we will use $\boldsymbol{r} = \boldsymbol{y} - \boldsymbol{x}$, in order to simplify the notation a bit.

The linearity of Stokes equation allows us to represent any distribution of body forces as a superposition of the point forces $\boldsymbol{g}$ we have introduced previously, an example of which is illustrated in Figure 2.2. In certain cases it is possible to uniquely determine the flow field inside a volume only in terms of the flows on its boundaries. This approach can be tackled via the boundary integral equations.

### 2.1.2 Boundary integral formulation of Stokes equations

In order to derive this boundary integral representation, we can rely on the Lorentz reciprocal identity [26] which states that in a fluid volume $V$ for two regular flows satisfying the Stokes equation $\boldsymbol{v}$ and $\boldsymbol{v'}$ along with their respective stress tensors $\boldsymbol{\sigma}$ and $\boldsymbol{\sigma'}$ we have

$$\frac{\partial}{\partial x_k}\left(v'_i \sigma_{ik} - v_k \sigma'_{ik}\right) = 0. \tag{2.9}$$

Setting the primed quantities to correspond to the fundamental solution of a point force introduced above

$$v'_i(\boldsymbol{x}) = \frac{1}{8\pi\eta} G_{ij}(\boldsymbol{x},\boldsymbol{y}) g_j, \quad \sigma'_{ik}(\boldsymbol{x}) = \frac{1}{8\pi} T_{ijk}(\boldsymbol{x},\boldsymbol{y}) g_j, \tag{2.10}$$

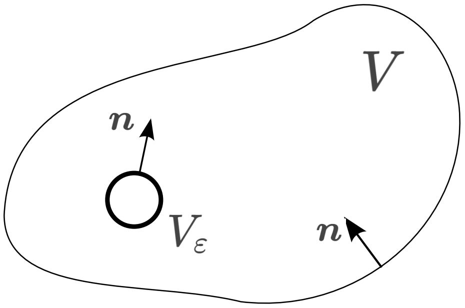

Figure 2.3: Integration over the droplet volume $V$, excluding a small spherical region $V_\varepsilon$ of radius $\epsilon$.

we arrive at

$$\frac{\partial}{\partial x_k}\left(\frac{1}{8\pi\eta}G_{ij}(\boldsymbol{x},\boldsymbol{y})g_j\ \sigma_{ik} - \frac{1}{8\pi}v_i T_{ijk}(\boldsymbol{x},\boldsymbol{y})g_j\right) = 0. \tag{2.11}$$

Since $\boldsymbol{g}$ is a constant vector, it is possible to drop it from this equation. Integrating (2.11) over the droplet volume $V^{(i)}$ bounded by S, except a small spherical volume $V_\epsilon$ bounded by $S_\epsilon$ of radius $\epsilon$ around the point force source at $\boldsymbol{y}$ to avoid running into singularities (shown in Figure 2.3), while remembering the divergence theorem

$$\int_V \boldsymbol{\nabla}\cdot\boldsymbol{A}\ dV = \int_S \boldsymbol{A}\cdot\boldsymbol{n}\ dS, \tag{2.12}$$

which is correct for smooth vector fields $\boldsymbol{A}$ over a volume $V$ and its smooth surface $\partial V$, we are able to arrive at

$$\int_{S,S_\epsilon}\left(\frac{1}{8\pi\eta^{(i)}}G_{ij}(\boldsymbol{x},\boldsymbol{y})\sigma_{ik} - \frac{1}{8\pi}v_i(\boldsymbol{x})T_{ijk}(\boldsymbol{x},\boldsymbol{y})\right)n_j(\boldsymbol{x})\ dS_x = 0. \tag{2.13}$$

Taking the radius of the excluded spherical region to zero $\epsilon \to 0$, it is found [27] that

$$\lim_{\epsilon\to 0}\int_{S_\epsilon}\frac{1}{8\pi\eta^{(i)}}G_{ij}(\boldsymbol{x},\boldsymbol{y})\sigma_{ik}n_j(\boldsymbol{x})\ dS_x = 0. \tag{2.14}$$

as well as for the second term

$$\lim_{\epsilon\to 0}\int_{S_\epsilon}\frac{1}{8\pi}v_i(\boldsymbol{x})T_{ijk}(\boldsymbol{x},\boldsymbol{y})n_j(\boldsymbol{x})\;dS_x=\begin{cases}-v_k(\boldsymbol{y}), & \boldsymbol{y}\in V^{(i)}\\ -\frac{1}{2}\;v_k(\boldsymbol{y}), & \boldsymbol{y}\in S\\ \quad 0, & \boldsymbol{y}\notin V^{(i)}\end{cases}\tag{2.15}$$

Gathering these results together, we see that

$$\int_S\left(\frac{1}{8\pi\eta^{(i)}}G_{ik}(\boldsymbol{x},\boldsymbol{y})\sigma_{ij}-\frac{1}{8\pi}v_i(\boldsymbol{x})T_{ijk}(\boldsymbol{x},\boldsymbol{y})\right)n_j(\boldsymbol{x})\;dS_x\;\begin{cases}-v_k(\boldsymbol{y}), & \boldsymbol{y}\in V^{(i)}\\ -\frac{1}{2}\;v_k(\boldsymbol{y}), & \boldsymbol{y}\in S\\ \quad 0, & \boldsymbol{y}\notin V^{(i)}\end{cases}\tag{2.16}$$

We can perform a similar analysis when integrating (2.11) over the volume of the surrounding carrier liquid $V^{(e)}$, which is bounded by the droplet surface denoted by $S$ and its own far away external boundary denoted by $S^\infty$:

$$\begin{aligned}&\int_S\left(\frac{1}{8\pi\eta^{(e)}}G_{ik}(\boldsymbol{x},\boldsymbol{y})\sigma_{ij}-\frac{1}{8\pi}v_i(\boldsymbol{x})T_{ijk}(\boldsymbol{x},\boldsymbol{y})\right)[-n_j(\boldsymbol{x})]\;dS_x\;+\\ &+\int_{S^\infty}\left(\frac{1}{8\pi\eta^{(e)}}G_{ik}(\boldsymbol{x},\boldsymbol{y})\sigma^\infty_{ij}-\frac{1}{8\pi}v^\infty_i(\boldsymbol{x})T_{ijk}(\boldsymbol{x},\boldsymbol{y})\right)n^\infty_j(\boldsymbol{x})\;dS_x=\\ &=\begin{cases}-v_k(\boldsymbol{y}), & \boldsymbol{y}\in V^{(e)}\\ -\frac{1}{2}\;v_k(\boldsymbol{y}), & \boldsymbol{y}\in S\\ \quad 0, & \boldsymbol{y}\notin V^{(e)}\end{cases}\end{aligned}\tag{2.17}$$

The first integral has a minus sign in front of its normal vector $n_j(\boldsymbol{x})$ to make it point out of the region of integration, as it the represents the normal vector of the droplet. The second integral in (2.17) is integrated over the far away boundary where the impact of the droplet is no longer felt, and so is simply equal to the background flow $v_{0k}(\boldsymbol{y})$.

We are, however, particularly interested in the velocity of the fluid interface, or equivalently the surface of the droplet, so we take the observation point $\boldsymbol{y}$ to lie on the interface $\boldsymbol{y} \in S$. Adding (2.16) multiplied by $\eta^{(i)}$ and (2.17) multiplied by $\eta^{(e)}$ we arrive at the boundary integral equation

$$\begin{aligned} v_k(\boldsymbol{y}) = \ & \frac{1}{4\pi(\eta^{(e)}+\eta^{(i)})} \int_S [\sigma_{ij}^{(e)} - \sigma_{ij}^{(i)}] \ G_{ik}(\boldsymbol{x},\boldsymbol{y}) n_j(\boldsymbol{x}) dS_x \\ & + \frac{1}{4\pi} \frac{\eta^{(e)}-\eta^{(i)}}{\eta^{(e)}+\eta^{(i)}} \int_S v_i(\boldsymbol{x}) T_{ijk}(\boldsymbol{x},\boldsymbol{y}) n_j(\boldsymbol{x}) dS_x \\ & + \frac{2\eta^{(e)}}{\eta^{(e)}+\eta^{(i)}} \ v_{0k}(\boldsymbol{y}), \end{aligned} \tag{2.18}$$

In further sections we will explore how to replace the stress tensor discontinuity of the first integral with the relevant boundary conditions in terms of surface tension and magnetic effects. When $\boldsymbol{y}$ lies on the boundary the functions in the integrands of (2.18) $G_{ik}$ and $T_{ijk}$ diverge as $\boldsymbol{x} \to \boldsymbol{y}$. In Section 3.3 we will explore options of *regularizing* these divergent integrands, so that they can be evaluated directly.

## 2.2 Equations governing the magnetostatics

In order to determine the behaviour of the magnetic fluid droplet, the magnetic fields needs to be known on its surface. As the involved magnetic field reacts to the changes of the droplet shape momentarily, the problem can be accurately assumed to be governed by magnetostatics.

We investigate the physical problem of a magnetic fluid droplet of magnetic permeability $\mu$ that is subjected to an external magnetic field $\boldsymbol{H_0}$.

Several assumptions are to be made in order to make the problem tractable. The droplet is assumed to be linearly magnetizable

$$\boldsymbol{M} = \chi \boldsymbol{H}, \tag{2.19}$$

where $\boldsymbol{M}$ is its magnetization, $\chi$ is the magnetic susceptibility and $\boldsymbol{H}$ is the magnetic field intensity.

We can express the magnetic field induction $\boldsymbol{B}$ as follows

$$\boldsymbol{B} = \mu_0(\boldsymbol{M} + \boldsymbol{H}) = \mu_0(\chi + 1)\boldsymbol{H} = \mu\boldsymbol{H}. \tag{2.20}$$

We assume the involved fluids to be non-conductive and so their free current densities $\boldsymbol{J}$ to be zero – the relevant Maxwell's equation [55] then reads:

$$\boldsymbol{\nabla} \times \boldsymbol{H} = \boldsymbol{J} = 0. \tag{2.21}$$

In this case the magnetic field can be expressed as a gradient of magnetic scalar potential $\psi$:

$$\boldsymbol{H} = \boldsymbol{\nabla}\psi. \tag{2.22}$$

From the Maxwell's equation

$$\boldsymbol{\nabla} \cdot \boldsymbol{B} = 0 \tag{2.23}$$

it follows that $\boldsymbol{\nabla} \cdot \boldsymbol{H} = 0$ if we also assume a uniform magnetic susceptibility $\chi$. These assumptions of non-existent free currents and uniform susceptibility allow us to conclude that the magnetic potential has to satisfy the Laplace equation

$$\boldsymbol{\nabla} \cdot \boldsymbol{\nabla}\psi = \Delta\psi = 0. \tag{2.24}$$

Considering the boundary equations on the fluid interface, denoted by $S$, it follows from the Maxwell's equations (2.21) and (2.23) that the magnetic field potential is continuous as is the normal component of the magnetic field induction $\boldsymbol{B}$ [56]

$$\psi^{(i)} = \psi^{(e)} \tag{2.25}$$

$$\mu\boldsymbol{\nabla}\psi^{(i)} \cdot \boldsymbol{n} = \boldsymbol{\nabla}\psi^{(e)} \cdot \boldsymbol{n}, \tag{2.26}$$

where $\boldsymbol{n}$ represents the outward-pointing normal vector of the droplet surface. The superscripts $(e)$ and $(i)$ here denote the parameters external and internal to the droplet, respectively. Finally, we expect the background magnetic field $\boldsymbol{H_0}$ far from the droplet to be unperturbed, $\boldsymbol{H}(\boldsymbol{r} \to \infty) = \boldsymbol{H_0}$, so we have another boundary condition on the magnetic scalar potential at infinity

$$\psi(\boldsymbol{r} \to \infty) = \boldsymbol{H_0} \cdot \boldsymbol{r}. \tag{2.27}$$

Taking these boundary conditions into account, the solution of the Laplace equation can be rewritten in an integral equation form, similarly to how we found the integral equation for velocity (2.18), [27]:

$$\psi(\boldsymbol{y}) = \frac{2\boldsymbol{H_0} \cdot \boldsymbol{y}}{\mu + 1} - \frac{1}{2\pi} \frac{\mu - 1}{\mu + 1} \int_S \psi(\boldsymbol{x}) \boldsymbol{\nabla}_x \left( \frac{1}{r} \right) \cdot \boldsymbol{n}(\boldsymbol{x}) \, \mathrm{d}S_x, \tag{2.28}$$

where the $\boldsymbol{H_0}$ term represents the undistorted background field and $r = |\boldsymbol{r}| = |\boldsymbol{y} - \boldsymbol{x}|$.

As we will see in further chapters, the droplet surface is described by a mesh of collocation points (nodes). The magnetic potential is calculated on the discrete mesh nodes, which allows us to calculate the tangential field component at each node

$$\boldsymbol{H_t} = (\mathbf{I} - \boldsymbol{n} \otimes \boldsymbol{n}) \cdot \nabla \psi, \tag{2.29}$$

where $\mathbf{I}$ is the identity matrix and $(\mathbf{I} - \boldsymbol{n} \otimes \boldsymbol{n})$ functions as a projection operator along the surface.

Since by definition the nodes lie precisely the surface of the droplet, it is not possible to directly obtain the normal component of the gradient of the magnetic potential. Therefore, to calculate the normal component of the field, we use an integral equation, where the normal field is expressed solely in terms of the tangential field component [43]:

$$\boldsymbol{H_n}(\boldsymbol{y}) = \frac{\boldsymbol{H_0} \cdot \boldsymbol{n}(\boldsymbol{y})}{\mu} - \frac{\mu - 1}{4\pi\mu} \boldsymbol{n}(\boldsymbol{y}) \cdot \mathcal{P} \int_S \left[ \big( \boldsymbol{n}(\boldsymbol{x}) \times \boldsymbol{H_t}(\boldsymbol{x}) \big) \times \boldsymbol{\nabla}_x \left( \frac{1}{r} \right) \right] \mathrm{d}S_x. \tag{2.30}$$

The integrand in (2.30) has a singularity of $O(1/r^2)$ when $\boldsymbol{x} \to \boldsymbol{y}$, so it should be evaluated as a Cauchy principal value integral represented by $\mathcal{P}$.

Solving this sequence of the boundary integrals yields the magnetic field intensity $\boldsymbol{H}$ on the droplet surface, from which we can recover the magnetic field induction $\boldsymbol{B}$ as well. This is useful, as the magnetizable droplet experiences a body force $\boldsymbol{f_M}$ due to being influenced by the magnetic field

$$f_{Mi} = \partial_k T_{ik}, \tag{2.31}$$

where $T_{ik}$ represents the Maxwell stress tensor [3, 57]

$$T_{ik} = -\frac{1}{2}\mu_0 H^2 \delta_{ik} + H_i B_k. \tag{2.32}$$

We will rely on (2.32) to construct the equations of motion of the droplet.

Looking at the normal force $f_n$ acting on a surface element because of the Maxwell stress tensor, we can find

$$\begin{aligned} f_n &= n_i T_{ik} n_k && (2.33)\\ &= -\frac{\mu_0 H_n^2}{2} - \frac{\mu_0 H_t^2}{2} + H_n B_n && (2.34)\\ &= -\frac{B_n^2}{2\mu_0} - \frac{\mu_0 H_t^2}{2} - \frac{\mu_0 M_n^2}{2} && (2.35)\end{aligned}$$

where the subscripts $t$ and $n$ refer to the tangential or normal components of the vectors respectively. In further sections we will rely on the normal force difference on the droplet surface

$$f_n^{(e)} - f_n^{(i)} = \frac{\mu_0 {M_n^{(i)}}^2}{2}, \tag{2.36}$$

where have utilized the fact that on the surface the $B_n$ and $H_t$ are continuous, and $M_n^{(e)}$ is equal to zero.

## 2.3 Equations of motion

We combine the hydrodynamic and magnetostatic models introduced in the previous chapter, to obtain the equations of motion for a droplet of magnetic fluid immersed in an infinite non-magnetic carrier fluid. Inertia of the fluids will be neglected and the fluids are modelled as incompressible.

In microfluidics the Reynolds number is approximately zero due to the small scales which allows to simplify the non-linear Navier-Stokes equation, so that the motion of the droplet is described by the Stokes equation for a magnetic fluid [3, 54]:

$$-\boldsymbol{\nabla} p + \eta \Delta \boldsymbol{v} + \boldsymbol{f_M} = \boldsymbol{0}, \qquad \boldsymbol{\nabla} \cdot \boldsymbol{v} = 0, \tag{2.37}$$

where $p$ is the pressure, $\eta$ is the dynamic viscosity, $f_{M\,i} = \partial_k T_{ik}$ is the volume force from the magnetic field introduced previously (2.31). It is possible to express this magnetic volume force $\boldsymbol{f_M}$ in terms of a gradient of a magnetic pressure $p_M$

$$\boldsymbol{f_M} = -\boldsymbol{\nabla} p_M \tag{2.38}$$

where $p_M$ can be found with some algebra, starting from the definition of the volume force ($f_{M\,i} = \partial_k T_{ik}$):

$$p_M = -\frac{\mu_0}{2}\left(\frac{\mu}{\mu_0} - 1\right) H^2 \tag{2.39}$$

This allows us to simplify the Stokes equations a bit

$$-\boldsymbol{\nabla} \tilde{p} + \eta \Delta \boldsymbol{v} = \boldsymbol{0}, \tag{2.40}$$

where $\tilde{p} = p + p_M$ is the effective pressure.

The force balance on the droplet boundary in the normal direction gives

$$n_i(\sigma_{ik}^{(e)} - \sigma_{ik}^{(i)})n_k + n_i(T_{ik}^{(e)} - T_{ik}^{(i)})n_k - \gamma(k_1 + k_2) = 0, \tag{2.41}$$

$$n_i(\sigma_{ik}^{(e)} - \sigma_{ik}^{(i)})n_k + \frac{\mu_0 {M_n^{(i)}}^2}{2} - \gamma(k_1 + k_2) = 0, \tag{2.42}$$

where $\sigma_{ik} = -p\delta_{ik} + \eta\left(\partial_i v_k + \partial_k v_i\right)$ is the stress tensor of the fluid, $M_n^{(i)}$ is the magnetization of the droplet, $\gamma(k_1 + k_2)$ is the capillary force due to the surface tension, $\gamma$ is the surface tension, $k_1, k_2$ are the principal surface curvatures, and $\boldsymbol{n}$ again is the unit normal vector directed out of the droplet.

Having introduced an effective pressure $\tilde{p}$, we have also indirectly introduced a modified effective stress tensor $\tilde{\sigma}_{ik} = -\tilde{p}\delta_{ik} + \eta\left(\partial_i v_k + \partial_k v_i\right)$. To express the boundary condition (2.42) in terms of $\tilde{\sigma}_{ik}$, we add and subtract $p_M$ from it and collect the remaining magnetic terms into a single effective magnetic surface force

$$f_M = \frac{\mu_0}{2}\left(\frac{\mu}{\mu_0} - 1\right) {H_t^{(i)}}^2 + \frac{\mu_0 {M_n^{(i)}}^2}{2} = \frac{\mu_0}{2}\left(\frac{\mu}{\mu_0} - 1\right)\left(\frac{\mu}{\mu_0}{H_n^{(i)}}^2 + {H_t^{(i)}}^2\right) \tag{2.43}$$

to finally arrive at the modified boundary condition in the normal direction

$$n_i(\tilde{\sigma}_{ik}^{(e)} - \tilde{\sigma}_{ik}^{(i)})n_k + f_M - \gamma(k_1 + k_2) = 0. \tag{2.44}$$

In the tangential direction we expect both the hydrodynamic and magnetic forces to be continuous across the droplet surface:

$$\begin{aligned} &t_i(\tilde{\sigma}_{ik}^{(e)} - \tilde{\sigma}_{ik}^{(i)})n_k = 0, \\ &t_i(T_{ik}^{(e)} - T_{ik}^{(i)})n_k = H_t^{(e)} B_n^{(e)} - H_t^{(i)} B_n^{(i)} = 0, \end{aligned} \tag{2.45}$$

where the second condition holds because both $H_t$ and $B_n$ are continuous across the boundary.

### 2.3.1 Equations of motion in integral form

We now obtain a modification of the velocity boundary integral equation of a point $\boldsymbol{y}$ on the droplet's surface (2.18) that automatically satisfies the force boundary conditions (2.44) and (2.45):

$$\begin{aligned} v_k(\boldsymbol{y}) = & \frac{1}{4\pi(\eta^{(e)}+\eta^{(i)})}\int_S f(\boldsymbol{x})n_i(\boldsymbol{x})G_{ik}(\boldsymbol{x},\boldsymbol{y})dS_x \\ & + \frac{1}{4\pi}\frac{\eta^{(e)}-\eta^{(i)}}{\eta^{(e)}+\eta^{(i)}}\int_S v_i(\boldsymbol{x})T_{ijk}(\boldsymbol{x},\boldsymbol{y})n_j(\boldsymbol{x})dS_x \\ & + \frac{2\eta^{(e)}}{\eta^{(e)}+\eta^{(i)}}\ v_{0k}(\boldsymbol{y}), \end{aligned} \tag{2.46}$$

where $\boldsymbol{v_0}$ is the background fluid flow and the integral is evaluated over the surface of the droplet.

The normal force on the surface in (2.46) reads

$$f = \left(\frac{1}{2}\mu_0\mu(\mu-1)H^{(i)2}_{n} + \frac{1}{2}\mu_0(\mu-1)H^{(i)2}_{t} - \gamma(k_1+k_2)\right), \tag{2.47}$$

where $H_t$ and $H_n$ are the tangential and normal components of the magnetic field on the surface, and $\mu$ is the relative permeability of the droplet.

## 2.4 Dimensionless variables and equations

A dimensionless variable or a dimensionless quantity is a quantity without a physical dimension ascribed to it, e.g. time or length, and its unit of measurement in the SI system is unity, usually not explicitly shown. For example in a simple pendulum system, we might measure the time in units of the oscillation periods of the system, that is, by rescaling the physical time elapsed with the characteristic period $t/T$.

Such dimensionless quantities are commonly used in science to clarify the description of various complex systems, which often have many interactions.

Here we propose the length scale as the radius of a spherical droplet $R_0$, time scale defined by $t_0 = R_0\eta^{(e)}/\gamma$, a magnetic field scale given by the external field $H_0$, a magnetic permeability scale given by the vacuum constant $\mu_0$, a viscosity parameter

$$\lambda = \eta^{(i)}/\eta^{(e)}, \tag{2.48}$$

and the Bond magnetic number

$$Bm = 4\pi\mu_0 R_0 H_0^2/\gamma. \tag{2.49}$$

The integral equation (2.46) can then be recast in a dimensionless form:

$$\begin{aligned} v_k(\boldsymbol{y}) = &-\frac{1}{1+\lambda}\frac{1}{4\pi}\int_S (k_1(\boldsymbol{x}) + k_2(\boldsymbol{x}))n_i(\boldsymbol{x})G_{ik}(\boldsymbol{x},\boldsymbol{y})dS_x \\ &+ \frac{1}{1+\lambda}\frac{1}{4\pi}\int_S f_M(\boldsymbol{x})n_i(\boldsymbol{x})G_{ik}(\boldsymbol{x},\boldsymbol{y})dS_x \\ &+ \frac{1-\lambda}{1+\lambda}\frac{1}{4\pi}\int_S v_i(\boldsymbol{x})T_{ijk}(\boldsymbol{x},\boldsymbol{y})n_j(\boldsymbol{x})dS_x \\ &+ \frac{2}{1+\lambda}v_{0k}(\boldsymbol{y}). \end{aligned} \tag{2.50}$$

The magnetic part of the normal force $f$ (2.47) can be isolated and in a dimensionless form gives [58]

$$f_M = \frac{Bm}{8\pi}(\mu - 1)\left(\mu {H^{(i)}}_n^2 + {H^{(i)}}_t^2\right). \tag{2.51}$$

## 2.5 Summary

This chapter has introduced the mathematical tools necessary to describe the hydrodynamic and magnetostatic problem of droplet dynamics. The essence of the theory could be summarized as follows – the linearity of Stokes equations allows us to construct a boundary integral equation for the surface velocity of the droplet from a distribution of surface forces, which combine the surface tension and magnetic forces.

# Chapter 3

# Numerical Algorithm

## Contents

The numerical algorithm developed and utilized during this thesis is explained in detail in this chapter. It is a generalization of [43] that limited their exploration of magnetic fluid droplets to their equilibrium configurations under the assumption of equal viscosities of the droplet and the surrounding carrier fluid.

## 3.1 Mesh representation

The magnetic fluid droplet surface is tessellated by a mesh of triangular boundary elements with collocation points (nodes) at their vertices. The integrals are calculated using the trapezoid integration method using only the integrand function values at the nodes. This approach allows us to conveniently recast the summation over the flat triangles to a summation over nodes [34]

$$\int_S f(\boldsymbol{x}) dS \approx \sum_i f(\boldsymbol{x}_i) \Delta S_i, \tag{3.1}$$

where the summation is done over every node $i$, and $\Delta S_i = 1/3 \sum \Delta S$ is the mean area of the triangles adjacent to the $i$-th node. The division by 1/3 arises from the fact that we evenly distribute one third of the contribution of each triangle to each of its vertices. Using this reformulation, the integral equations become simply linear systems of equations that can be solved with common numerical libraries. Solution of the integral equations of §2 produces the velocities of each node and allows us to calculate the dynamics of the droplet surface.

The original spherical mesh is obtained by iteratively “slicing” an icosahedron, by adding more nodes on its faces and projecting the newly added nodes on a sphere, as shown in Figure 3.1, and proposed in [59]. The simulations usually utilized two or three slicing iterations, increasing the number of nodes up to 162 or 642 respectively. The normals and the surface curvatures at each vertex are determined by fitting a paraboloid on the relevant vertex and its immediate neighboring vertices [34].

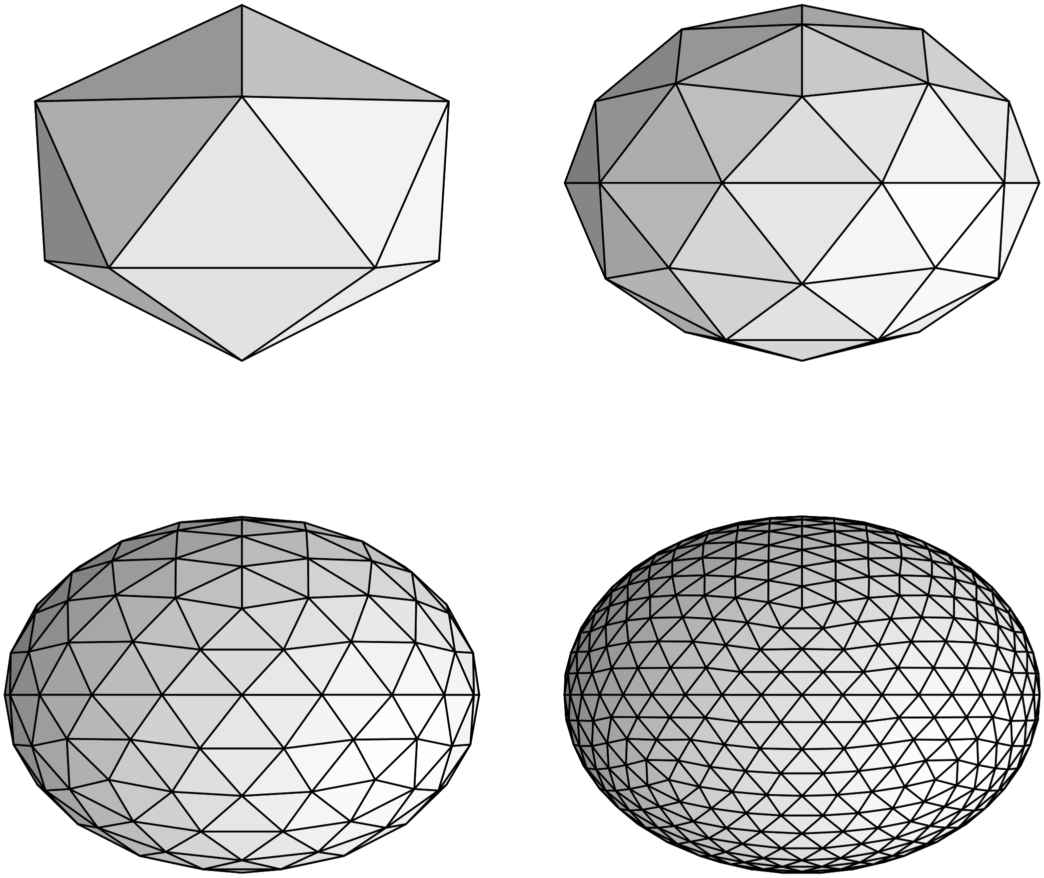

Figure 3.1: Mesh generation procedure. An icosahedron can be iteratively sliced to produce a mesh of desired resolution. Our simulations typically started with two (bottom left) or three (bottom right) slicings, yielding 162 or 642 nodes respectively.

## 3.2 Mesh maintenance

In general, the droplet surface has a nonuniform velocity distribution, so just translating the initially uniformly distributed nodes would degrade the mesh quality rather fast, as some triangles would become more deformed than others.

To diminish this unwanted effect, numerous mesh maintenance techniques are used during the simulations, which are explained in this section.

### 3.2.1 Passive stabilization

Given that the dynamics of the droplet surface is determined solely by the normal velocity component, the mesh degradation may be slowed by properly adjusting the tangential velocity components. In the so called *passive* stabilization [35], the tangential components can be adjusted in order to minimize a certain "kinetic energy" function

$$F = \sum_{\boldsymbol{x}_{ij}} \left[ \frac{d}{dt} \left( \frac{|\boldsymbol{x}_{ij}|^2}{h_{ij}^2} + \frac{h_{ij}^2}{|\boldsymbol{x}_{ij}|^2} \right) \right]^2 + 0.4 \sum_{\Delta} \frac{1}{C_\Delta^2} \left( \frac{dC_\Delta}{dt} \right)^2, \tag{3.2}$$

where the first sum pertains to edges between nodes $i$ and $j$ and tries to keep the edges $\boldsymbol{x}_{ij}$ at some optimal length $h_{ij}$ that is determined by the local curvatures of each node [35], while the second sum pertains to the mesh surface triangles and attempts to keep the triangles as regular as possible, by using the "compactness" of a triangle

$$C_\Delta = \frac{S_\Delta}{a^2 + b^2 + c^2}, \tag{3.3}$$

with $a, b, c$ representing the triangle side lengths, as a guide [35].

### 3.2.2 Active stabilization

The algorithm outlined above slows the mesh degradation but does not stop it entirely. In addition the so called *active* stabilization [35] between the time-stepping of nodes is necessary. In *active* stabilization the nodes are translated along the surface of the droplet in order to attempt to minimize a "potential energy" function

$$E = \sum_{\boldsymbol{x}_{ij}} \left[ \frac{1}{2} \left( \frac{|\boldsymbol{x}_{ij}|^2}{h_{ij}^2} + \frac{h_{ij}^2}{|\boldsymbol{x}_{ij}|^2} \right) \right]^{50} + \sum_{\Delta} \left( \frac{C_\Delta^{reg}}{C_\Delta} \right)^{100}, \tag{3.4}$$

where $C_\Delta^{reg} = \sqrt{3}/12$ is the compactness value of a regular triangle. This "potential energy" function $E$ takes on large values when an edge $\boldsymbol{x}_{ij}$ differs a lot from its optimal length of $h_{ij}$ and so it avoids both inappropriate crowding and scattering of vertices, as well not allowing triangles to deviate a lot from the optimal compactness value of a regular triangle. In order to move the node $\boldsymbol{x}^i$ along the surface of the droplet, we utilize the previously fitted paraboloid that was used in the normal vector calculations with $\boldsymbol{x}^i$ lying at the tip of the paraboloid. This paraboloid locally approximately coincides with the droplet surface, as described by the nearby vertices. The node $\boldsymbol{x}^i$ is then translated along this surface so as to minimize the "potential energy" $E$.

The above energy functions $E$ and $F$ have their gradients expressible in an explicit analytical form, allowing for efficient calculations. To find the minimum of $F$ we rely on the conjugate gradient method [60]. To minimize $E$, we rely on a modified gradient descent method, where after each step the points are projected back on the paraboloid that approximately describes the local droplet surface [35].

### 3.2.3 Edge flipping

Edges between vertices can be reconnected. Consider a quadrilateral described by vertices $\left[\boldsymbol{x}^a, \boldsymbol{x}^b, \boldsymbol{x}^d, \boldsymbol{x}^c\right]$ with an additional edge, connecting the two diagonally opposite vertices $\left[\boldsymbol{x}^a, \boldsymbol{x}^d\right]$.

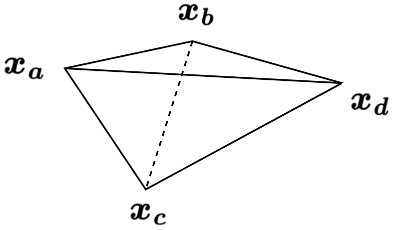

Figure 3.2: Edges might be flipped to create more regular triangles.

This edge might be flipped to instead connect the vertices $\left[\boldsymbol{x}^b, \boldsymbol{x}^c\right]$, as shown in Figure 3.2, given that

$$\left|\boldsymbol{x}^b - \boldsymbol{x}^c\right|^2 < \left|(\boldsymbol{x}^b - \boldsymbol{O}^b)(\boldsymbol{x}^c - \boldsymbol{x}^b)\right| + \left|(\boldsymbol{x}^c - \boldsymbol{O}^c)(\boldsymbol{x}^c - \boldsymbol{x}^b)\right|,$$

with $\boldsymbol{O}^k$ describing the circumcenter of the triangle $\left[\boldsymbol{x}^a, \boldsymbol{x}^d, \boldsymbol{x}^k\right]$, where $k \in \{b, c\}$ [35, 36]. These edge flips allow for increasingly regular triangles and they are applied sequentially to all of the edges until no more flips are allowed. There are extra rules, however — an edge will not be flipped, if it would result in a node with less than five connected neighbouring nodes. This is enforced to ensure that a general paraboloid, requiring five parameters describing its shape, can be fitted to every node and its neighbors. The edge flipping algorithm is applied at every simulation step. If any edge has been flipped, *active* stabilization will be applied again to ensure the regularity of the mesh.

### 3.2.4 Node addition

It was found that to ensure accurate results, more nodes are needed in regions of high curvature than can be supported with the techniques introduced above, therefore, we also implement a node addition routine. At each vertex, we have to compute the magnitude of curvature

$$H = \sqrt{k_1^2 + k_2^2}, \tag{3.5}$$

where $k_1, k_2$ are the principal curvatures, calculated from the previously fitted paraboloids. The magnitude of the curvature is a better measure than the mean curvature, as in the average approach the curvatures might cancel each other out in regions where the droplet shape resembles a hyperbolic paraboloid.

Then for each triangle we calculate the mean curvature of its vertices $H_\Delta = \frac{1}{3}\sum\limits_{i\in\Delta} H_i$ as well as the square root of its area $\sqrt{S_\Delta}$, signifying the characteristic length scale of the triangle. Each triangle for which $H_\Delta\sqrt{S_\Delta} > \varepsilon$ is marked for node addition, with $\varepsilon$ being an empirically determined cut-off criteria. Moreover, if a triangle has two or more neighboring triangles marked for splitting, it itself is also marked.

To determine a sufficiently optimal $\varepsilon$ value, a droplet was elongated in a constant field with various $\varepsilon$ values and the ratio of the droplet semi-axes evolution compared (Figure 3.3). The semi-axes here refer to the longest and shortest axes of an ellipsoid, fitted to the droplet shape. A threshold for cut-off value of 0.2 was found to be sufficient for a precision of $10^{-3}$. The smaller the value of $\varepsilon$, the more quickly the number of nodes is increased, as demonstrated in Figure 3.4. This significantly increases the time of computation, which scales approximately as $O(N^2)$, where $N$ is the number of nodes. Unless stated otherwise, the cut-off of $\varepsilon = 0.2$ is used in further simulations.

New nodes will be introduced at the middle of each edge of the marked triangles [36]. These new nodes are then mutually connected so that each of them has at least five neighbours. Again, this is to ensure that a general paraboloid will be fittable upon every node.

To ensure the smoothness of the surface, every added node is projected on a paraboloid of one the original vertices. The paraboloid chosen for projection is that

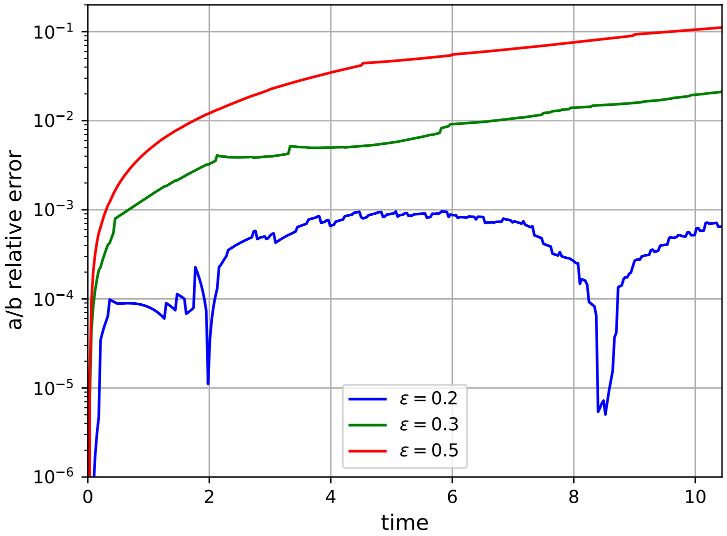

Figure 3.3: The relative error of the axis ratio, as compared to the $\varepsilon = 0.15$ case. Unless stated otherwise, in further simulations $\varepsilon = 0.2$ was used, as its relative error of $10^{-3}$ (blue curve) was deemed to be acceptable. In these simulations, a droplet of $\lambda = 1$ and $\mu = 22$ was elongated in a magnetic field of $Bm = 5.8$. This figure has been obtained in collaboration with A. P. Stikuts.

whose corresponding node is the closest to the newly added node.

Finally, the neighborhood of triangles affected by this new node addition is also *actively* stabilized, similarly as in [36]. The node addition routine is shown in Figure 3.5.

## 3.3 Regularization of the boundary integral equations

The integral equations introduced in 2 have their integrands often divergent as $\boldsymbol{x} \to \boldsymbol{y}$ which poses difficulties to their numerical calculation at those points. This behaviour

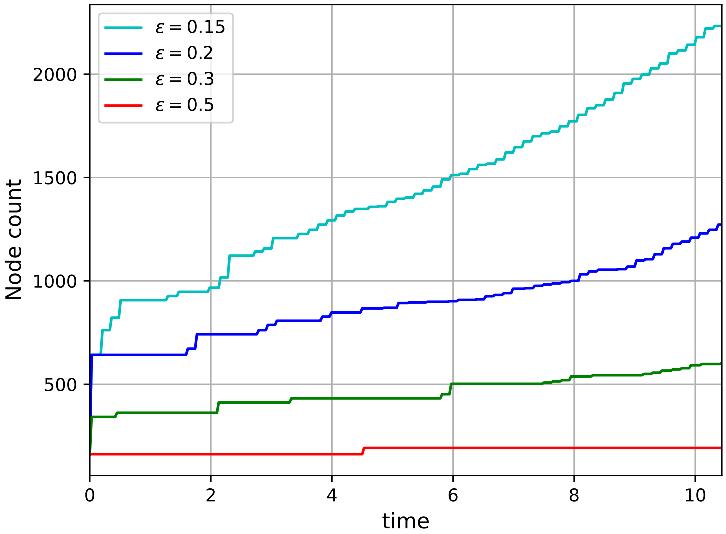

Figure 3.4: The number of nodes in time for various values of the cut-off criterion $\varepsilon$, corresponding to the simulations shown in Fig. 3.3. This figure has been obtained in collaboration with A. P. Stikuts.

can be handled by *regularizing* the integrands, so that they are no longer divergent at all or they have been made weakly singular and can then be handled using some simple approaches [61, 62]. These techniques are explained in this section.

### 3.3.1 Regularization of the velocity integral equation

Every integrand shown in (2.50) is weakly singular, meaning that their scaling follows $O(1/r)$, with $\boldsymbol{r} = \boldsymbol{x} - \boldsymbol{y}$, as $\boldsymbol{x} \to \boldsymbol{y}$ and are thus convergent. This scaling behavior can be determined by expanding the integrands in Taylor series for small $\boldsymbol{r}$ in a local coordinate system centered at $\boldsymbol{y}$. It may also be noted that $\boldsymbol{r} \cdot \boldsymbol{n} = O(r^2)$ as $\boldsymbol{x} \to \boldsymbol{y}$. These integrals can be handled numerically, for example, by integrating them on the singular elements in polar coordinates (centered around the divergent node $\boldsymbol{y}$), where a factor of $r$ arises from the differential area element ($dS = r dr d\theta$), cancelling

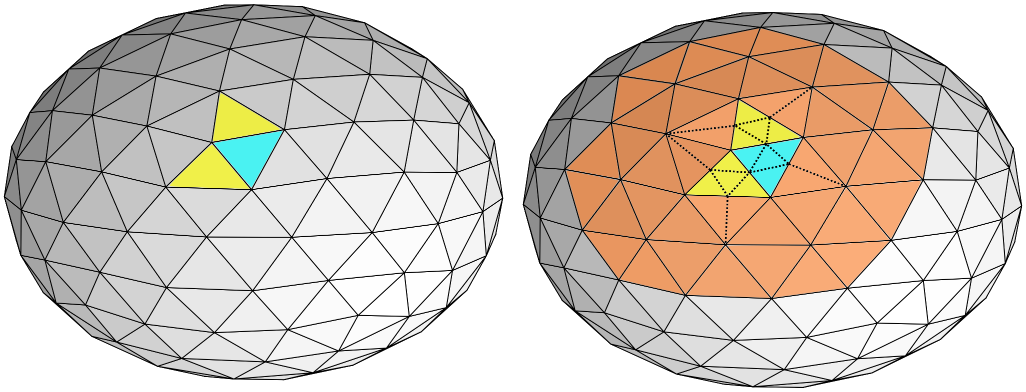

Figure 3.5: An illustrative example of the node addition routine. First, the triangles marked for node addition are found, as shown in yellow. As the cyan triangle has at least two neighboring triangles marked for splitting, it itself is also marked. The new nodes are added in the middle of every edge of the marked triangles, remembering to introduce extra edges to make sure every node has at least five neighbors. The new edges are indicated by the dashed lines. Finally, the affected triangles as well as their neighborhood, marked in orange, are *actively* stabilized to enhance the mesh quality.

out the $1/r$ singularity discussed above [26]. However, an easier implementation with a greater precision of the numerical scheme can be obtained by removing these singularities altogether, which is possible for these integrals.

Since the first integral in (2.50) is calculated over a closed surface, it may be transformed in the following form [63]

$$\begin{aligned}\int_S (k_1(\boldsymbol{x})+k_2(\boldsymbol{x}))n_i(\boldsymbol{x})G_{ik}(\boldsymbol{x},\boldsymbol{y})dS_x = \\ -\int_S \Bigg( r_i n_i(\boldsymbol{x})n_k(\boldsymbol{y}) + r_i n_i(\boldsymbol{y})n_k(\boldsymbol{x}) + (1-n_i(\boldsymbol{x})n_i(\boldsymbol{y}))r_k \\ - \frac{3r_k(n_i(\boldsymbol{x})+n_i(\boldsymbol{y}))r_i r_j n_j(\boldsymbol{x})}{|\boldsymbol{r}|^2}\Bigg)\frac{dS_x}{|\boldsymbol{r}|^3},\end{aligned} \tag{3.6}$$

This transformation leads us to the term in the brackets scaling as $|\boldsymbol{r}|^3$ and making the whole integrand scale as $O(1)$, as $\boldsymbol{x} \to \boldsymbol{y}$. Moreover, computing the sum of principal curvatures $(k_1 + k_2) = \boldsymbol{\nabla} \cdot \boldsymbol{n}$ in the integral on the left hand side of (3.6) famously introduces large errors due to the surface discretization [34, 63], which in this new form is now avoided.

The singularity of the second integrand in (2.50) can be reduced by an order using the method of singularity subtraction [27]. We use the identity [43]

$$\int_S n_i(\boldsymbol{x})G_{ik}(\boldsymbol{x},\boldsymbol{y})dS_x = 0, \tag{3.7}$$

which we multiply with the magnetic force $f_M(\boldsymbol{y})$ and subtract it from the second integral in (2.50) to get

$$\int_S f_M(\boldsymbol{x})n_i(\boldsymbol{x})G_{ik}(\boldsymbol{x},\boldsymbol{y})dS_x = \int_S [f_M(\boldsymbol{x}) - f_M(\boldsymbol{y})]n_i(\boldsymbol{x})G_{ik}(\boldsymbol{x},\boldsymbol{y})dS_x, \tag{3.8}$$

whereby now the integrand on the right hand side is no longer singular as $\boldsymbol{x} \to \boldsymbol{y}$, but rather $O(1)$, if $f_M(\boldsymbol{x})$ is a smooth function.

Finally, the last integral in (2.50) can also be treated with singularity subtraction by making use of the identity [27]

$$\int_S T_{ijk}(\boldsymbol{x},\boldsymbol{y})n_j(\boldsymbol{x})dS_x = -4\pi\delta_{ik} \tag{3.9}$$

and is replaced by

$$\int_S v_i(\boldsymbol{x})T_{ijk}(\boldsymbol{x},\boldsymbol{y})n_j(\boldsymbol{x})dS_x = \int_S [v_i(\boldsymbol{x}) - v_i(\boldsymbol{y})]\, T_{ijk}(\boldsymbol{x},\boldsymbol{y})n_j(\boldsymbol{x})dS_x - 4\pi v_k(\boldsymbol{y}). \tag{3.10}$$

As a result the order of the singularity has been reduced by one, and the integrand stays bounded as $\boldsymbol{x} \to \boldsymbol{y}$, if $v_i(\boldsymbol{x})$ is a smooth function.

We can rewrite the integral equation (2.50) for $\boldsymbol{v}$ in the form

$$v_k(\boldsymbol{y}) = \frac{\kappa}{4\pi} \int_S v_i(\boldsymbol{x}) T_{ijk}(\boldsymbol{x}, \boldsymbol{y}) n_j(\boldsymbol{x}) dS_x + F_k(\boldsymbol{y}), \tag{3.11}$$

where $\boldsymbol{F}$ is a function independent of $\boldsymbol{v}$ and $\kappa = \frac{1-\lambda}{1+\lambda}$. It is known [64] that the homogeneous part of this integral equation has eigensolutions with eigenvalues $\kappa = \pm 1$. The $\kappa = 1$ eigensolution corresponds to a uniform expansion of the droplet and the $\kappa = -1$ eigensolution corresponds to an arbitrary rigid body motion of it. Hence, in cases where $\lambda \gg 1$ or $\lambda \ll 1$ the integral equation is poorly determined. Magnetic droplets produced by a demixing of magnetic colloids have been observed to have large viscosities ($\lambda \approx 100$ [7]). Therefore, we use Wielandt's deflation [64], an approach where we formulate an equivalent integral equation that has the unwanted eigensolutions removed.

### 3.3.2 Regularization of the magnetostatic integral equations

Similarly as before with the velocity integral equations, singularity subtraction is applied, making use of identities

$$\int_S \frac{1}{4\pi} \boldsymbol{\nabla}_x \left(\frac{1}{r}\right) \cdot \boldsymbol{n}(\boldsymbol{x}) \, \mathrm{d}S_x = -\frac{1}{2}, \tag{3.12}$$

$$\int_S \frac{\boldsymbol{n}(\boldsymbol{x}) \times \boldsymbol{r}}{r^3} \mathrm{d}S_x = \boldsymbol{0}, \tag{3.13}$$

where $\boldsymbol{r} = \boldsymbol{y} - \boldsymbol{x}$ and $\boldsymbol{y}$ is located on the boundary of the region of integration.

The equation of the magnetic potential can be also rewritten in a regularized form by means of (3.12):

$$\psi(\boldsymbol{y}) = \boldsymbol{H_0}(\boldsymbol{y}) \cdot \boldsymbol{y} - \frac{\mu - 1}{4\pi} \int_S \left[\psi(\boldsymbol{x}) - \psi(\boldsymbol{y})\right] \boldsymbol{\nabla}_x \left(\frac{1}{r}\right) \cdot \boldsymbol{n}(\boldsymbol{x}) \, \mathrm{d}S_x. \tag{3.14}$$

The relation for the normal field component is also regularized by using (3.12) and (3.13) [43] (note: here the sign is opposite in front of the integral term as compared to that in Eq. (3.9) of [43]):

$$H_n(\boldsymbol{y}) = \frac{\boldsymbol{H_0} \cdot \boldsymbol{n}(\boldsymbol{y})}{\mu} - \frac{\mu - 1}{4\pi\mu}\, \boldsymbol{n}(\boldsymbol{y}) \cdot \int_S \Bigg[ [\boldsymbol{H_t}(\boldsymbol{x}) - \boldsymbol{H_t}(\boldsymbol{y})]\ \boldsymbol{\nabla}_x \left(\frac{1}{r}\right) \cdot \boldsymbol{n}(\boldsymbol{x}) - [\boldsymbol{H_t}(\boldsymbol{x}) - \boldsymbol{H_t}(\boldsymbol{y})] \times \left( \boldsymbol{n}(\boldsymbol{x}) \times \boldsymbol{\nabla}_x \left(\frac{1}{r}\right) \right) \Bigg] \mathrm{d}S_x.$$

Analogously as was the approach of the velocity calculation, the integrands in the regularized equations are now bounded as $\boldsymbol{x} \to \boldsymbol{y}$, and can easily be integrated using numerical methods. Here again singular integrands are calculated using local polar coordinates centered at $\boldsymbol{y}$ for the singular elements [26, 43].

We have also derived an alternative approach for obtaining the normal and tangential field components using the normal field differences on the surface, but it was observed to be less accurate and slower than the approaches introduced above. Consequently this alternative approach was not used in further calculations. For details, refer to Appendices A.1 and A.2.

After solving these boundary integral equations for the magnetic field, the forces acting of the droplet surface (2.47) can be obtained and afterwards the velocity of each mesh node can be found.

## 3.4 Time integration scheme

It was found that space–discretization has a larger impact on convergence of the simulations rather than time–discretization.

Consequently, a classic first-order Euler method for time integration is utilized. Nonetheless, this method does not preserve the droplet volume – it accumulates small volume changes at each time step. This can be remedied by rescaling the droplet volume after every iteration. Our algorithm relies on an adaptive time step $\Delta t$ inspired by [65]

$$\begin{gathered}\Delta\tau = 7.4 \text{ min} \left\{ \left( \frac{\Delta x_{min}}{|k|_{max}} \right)_i \right\} \\ \Delta t = \text{min} \left\{ \Delta\tau,\ 0.05\frac{2\pi}{\omega},\ 0.07 \right\}\end{gathered}, \tag{3.15}$$

where $\Delta x_{min}$ is the shortest edge length connected to the $i$-th node, and $|k|_{max}$ is the largest absolute value of principal curvature at the $i$-th node, and $\omega$ is the dimensionless rotation frequency of the magnetic field.

## 3.5 Summary

The numerical algorithm can be briefly summarized as follows:

- For a particular external magnetic field, solve the boundary integral equation for the magnetic potential $\psi$ on the droplet surface (3.14).
- Find the tangential field component $\boldsymbol{H_t} = (I - \boldsymbol{n} \otimes \boldsymbol{n})\ \nabla\psi$.
- Determine the normal field component $\boldsymbol{H_n}$ in a regularized form in terms of the tangential component using (2.30).
- Calculate the normal magnetic surface forces $\boldsymbol{f_M}$ (2.51).
- Obtain the velocities of each node from the integral equation (2.50) and translate them accordingly with the first-order Euler method, after adjusting for the optimal tangential velocity component via *passive* stabilization.
- Rescale the droplet volume, to compensate the discrepancies introduced by the Euler method.

- Apply mesh maintenance by node addition and flipping of edges at every simulation step, as well as the *active* stabilization every hundred simulation steps. However, if any nodes have been added or any edges have been flipped, perform active stabilization immediately.

In the integral equation formulation the magnetic quantities and the velocity at each mesh node depend on contributions from all the other nodes. This means that the time required to determine the effects of every node scales as $O(N^2)$, where $N$ is the number of mesh nodes. Populating the matrices corresponding to the integral operators takes up most of the time at every simulation step. Nonetheless, this can be sped up by using parallel computation methods.

# Chapter 4

# Algorithm validation

## Contents

Having introduced the algorithm itself and its mesh stabilization techniques, we now turn to validating its outputs with multiple known theoretical relationships for magnetic fluid droplet equilibrium configurations and dynamics. The situation we look at in the hydrodynamical case concerns the relaxation to a sphere of an initially elongated droplet without a background magnetic field. The cases with a magnetic field present will consist of the comparison of droplet elongation versus the expected deformation in an external magnetic field, as well as the test of whether the algorithm is able to capture the hysteresis behaviour of the droplet in increasing and later decreasing magnetic field. Moreover, we will also check if the algorithm correctly estimates the characteristic time scaling that is spent in the quasi-stable bottleneck region before undergoing a sudden elongation as is expected from the theoretical considerations.

A challenging aspect of this validation part is the limited availability of theoretical relationships, as the magnetic fluid droplet problem is rather difficult and is not easily tractable with analytical tools.

Discrepancies between these theoretical relations and our numerical simulation results might hint at the limits of applicability of the relations themselves or the limits of the assumptions underlying their derivations. An example of a notable assumption to be tested is the assumption of the ellipsoidal shape of the droplet, as we will see below.

## 4.1 Relaxation to a sphere

A stretched droplet approximated with an ellipsoid of rotation can be described by the Taylor deformation parameter parameter

$$D = \frac{a-b}{a+b}, \tag{4.1}$$

where $a$ and $b$ represent its major and minor semi-axis respectively. In the absence of an external magnetic field, small elongations should decay exponentially under the action of capillary forces $D \propto e^{-t/\tau}$, where the characteristic relaxation time $\tau$, rescaled by the time scale of the system, reads [66]:

$$\frac{\tau}{\eta^{(e)} R_0/\gamma} = \frac{(16+19\lambda)(3+2\lambda)}{40(1+\lambda)}. \tag{4.2}$$

A comparison with the numerically determined relaxation times is presented in Figure 4.1.

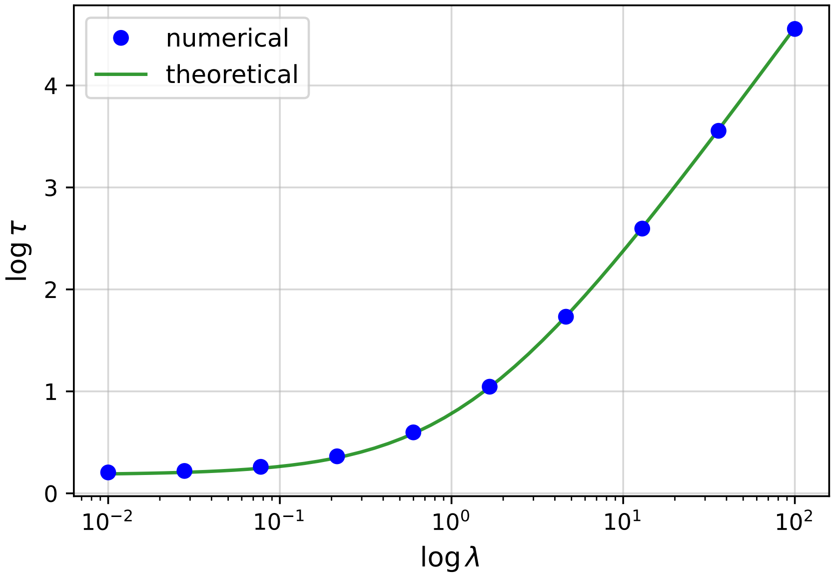

Figure 4.1: Characteristic dimensionless relaxation time $\tau$ of an elongated droplet as a function of the droplet-fluid viscosity ratio $\lambda$. The points are the numerical results that closely follow the analytical curve (4.2). The magnetic effects are not relevant in this simple relaxation case. This figure has been obtained in collaboration with A. P. Stikuts.

## 4.2 Equilibrium elongation in constant field

We can further compare the equilibrium configurations determined by the algorithm against relations given below. Figure 4.2 exhibits the comparison between the numerically obtained equilibrium shapes of the droplet in a given magnetic field $Bm$ with the theoretical relationship from [5, 13]

$$Bm = \left[\frac{4\pi}{\mu - 1} + N\right]^2 \frac{1}{2\pi} \frac{\left(\frac{3-2e^2}{e^2} - \frac{(3-4e^2)\arcsin e}{e^3(1-e^2)^{1/2}}\right)}{(1-e^2)^{2/3}\left(\frac{(3-e^2)}{e^5}\log\left(\frac{1+e}{1-e}\right) - \frac{6}{e^4}\right)}, \tag{4.3}$$

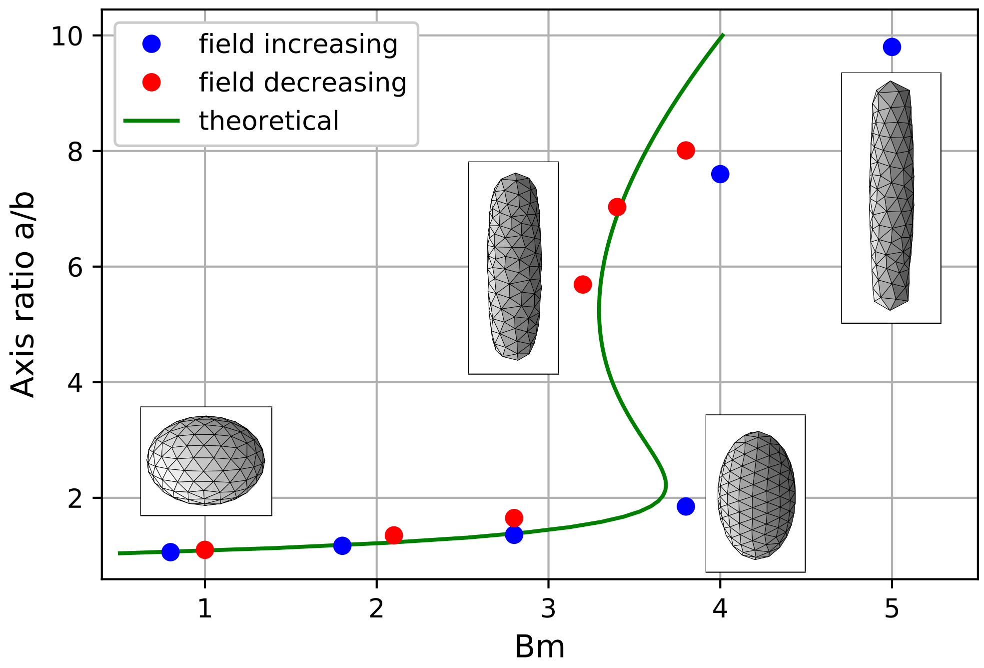

Figure 4.2: Evolution of the droplet through the hysteresis region. The blue (red) points indicate the calculated trajectory with increasing (decreasing) magnetic field once the droplet has equilibriated. The simulation utilized $\mu = 30$ and $\lambda = 7.6$.

where $e$ symbolizes the eccentricity of the fitted ellipsoid $e = \sqrt{1 - b^2/a^2}$ with $a,\ b$ being its long and short semi-axis, respectively, and $N$ is the demagnetizing factor that for prolate ellipsoids reads [54]

$$N = \frac{4\pi(1-e^2)}{2e^3}\left(\log\frac{1+e}{1-e} - 2e\right). \tag{4.4}$$

The derivation of the equilibrium formula (4.3) relies on an assumption of an axisymmetric ellipsoidal droplet, an approximation which works well until the axial ratio of about 7 [6]. This limit can also be observed in Fig. 4.2 where the simulated result deviates for highly elongated droplets, an effect explained by the droplet developing more conical tips than a fitted ellipsoid would possess at the corresponding elongation, and thus no longer obeying to the ellipsoidal approximation.

When the simulation approaches the equilibrium, the collocation nodes are translated by increasingly smaller displacements. In order to achieve the $t \to \infty$ behaviour of the axis ratio $a/b$, the equilibriated points shown in Figure 4.2 are found by the Shanks transformation [67].

There is a bifurcation in the equilibrium curve (4.3) that appears with larger permeability $\mu$ values. At a permeability value $\mu \gtrsim 21$ the equilibrium curve becomes multivalued with respect to magnetic field, indicating an instability onset (Figure 4.2). Instability here refers to the situation where for a single magnetic field value there are multiple axis ratio values, indicating multiple simultaneous available equilibria. For example, if in this case with $\mu = 30$, the magnetic field $Bm$ is increased past the critical value, $Bm_c \approx 3.68$, the droplet configuration becomes unstable (as it no longer stays "on" the equilibrium curve) and has to "jump" to another stable configuration, on the right side of Figure 4.2, i.e. suddenly stretch.

After the droplet has reached this new stable configuration, the field can be lowered below the critical value now, however the droplet will not "jump" back (contract) to its previously stable configuration, but rather trace the equilibrium curve. This phenomenon is called hysteresis, whereby the system returns to a different state other than its original, when external perturbing forces have returned to their initial pre-perturbation values.

With lower magnetic field values, the droplet shape would trace the curve until a second critical magnetic field value of around $Bm \approx 3.32$ (for $\mu = 30$) is achieved. With even lower fields, the droplet would once again suddenly "jump" back (contract) to return to a stable configuration again. Figure 4.2 displays the path of hysteresis calculated by the algorithm. In these simulations the node addition technique was deactivated since accurate description of such highly stretched droplets would require exceedingly many points. Nonetheless, other mesh stabilization techniques were still employed, and so the simulation results here allow only for qualitative interpretation.

## 4.3 Elongation of quasi-stable droplets

### 4.3.1 Elongation bottleneck

The smaller the amount the magnetic field is over the critical value, the longer the droplet will stay in this quasi-stable state, before it "jumps" over to a truly stable configuration, indicating a time bottleneck region.

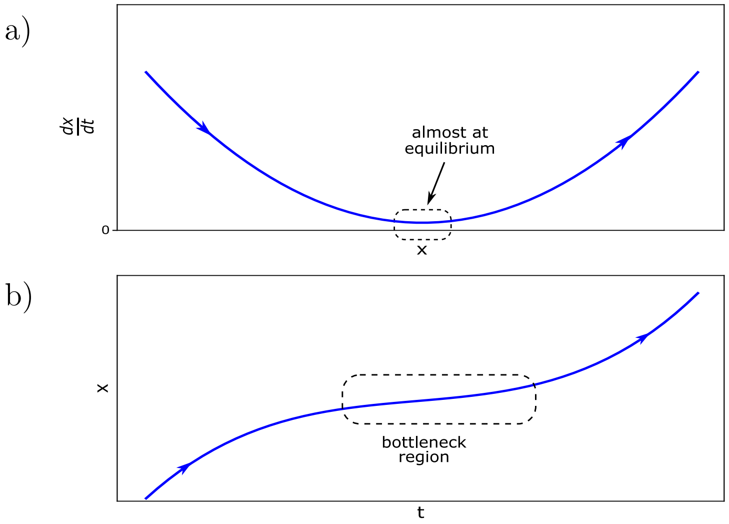

Figure 4.3: The evolution (indicated by arrows) of a dynamical system described by some parameter $x$ near an equilibrium point. As the system evolves through the equilibrium neighbourhood shown in Fig. a), its velocity is almost zero, as it has *almost* reached a fixed point. Therefore, the system will take a long time to get through this region, creating the time bottleneck $\tau$, shown in Fig. b), that usually scales as $\tau \sim d^{-1/2}$, where $d$ is the distance to the fixed point [68].

An illustration and explanation of this bottleneck behaviour in terms of an abstract dynamical system describing the evolution of some parameter $x$ is given in Figure 4.3. The dynamics of this instability "jump" are governed by a hyperbolic differential equation shown by [15] for small $t$

$$\frac{a}{b} - \left(\frac{a}{b}\right)_c = S\ \tau \tan\frac{t}{\tau}, \tag{4.5}$$

where $a/b$ is semi-axial length ratio, here $\tau$ is the characteristic time spent in the bottleneck region before the "jump", $t$ represents time, $S$ is a numerical constant, and the subscript $c$ indicates critical value, i.e. the one at the extremum of the equilibrium curve (4.3).

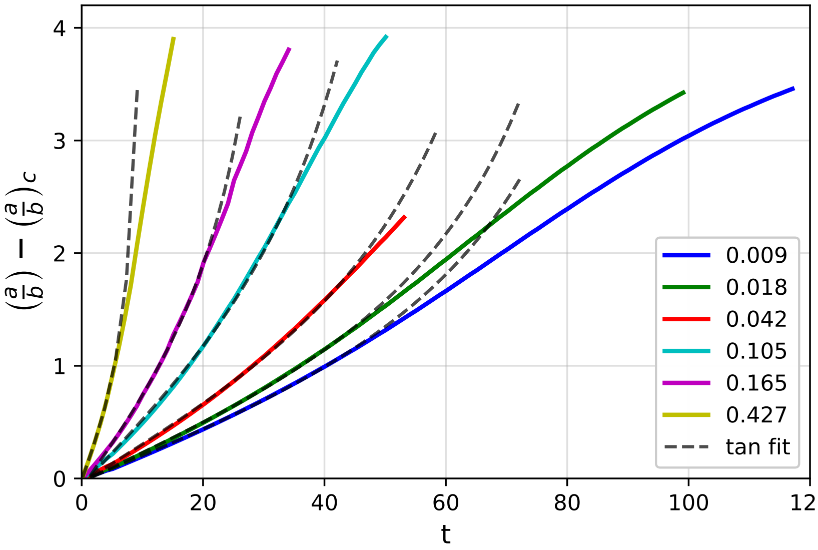

Figure 4.4: Elongations of the droplet during "jumping over" the hysteresis region at various external magnetic field $h$ values, with an overlay of dashed tangential fits, according to (4.5). The originally accelerated dynamics saturate as the droplet reaches its new equilibrium elongation. Droplet parameter values used in simulations here were $\mu = 30, \lambda = 7.6$.

An example of multiple droplet stretching trajectories at different magnetic fields $h = H/H_c - 1$ is shown in Figure 4.4, with the corresponding tangential fits of Eq. (4.5) of $\tau$ and $S$ overlayed with the dashed lines. These trajectories were obtained by subjecting an ellipsoidal droplet ($\mu = 30,\ \lambda = 7.6$) stretched to the corresponding critical (pre-hysteresis "jump") axis ratio of $a/b = 2.21$ and letting it evolve in various field strengths. It can be seen that the initially slow dynamics of the "bottleneck" region are followed by a relatively fast stretching – the "jump" – and is finally saturating into a new equilibrium position (most noticeably exemplified by the dark blue curve in Figure 4.4).

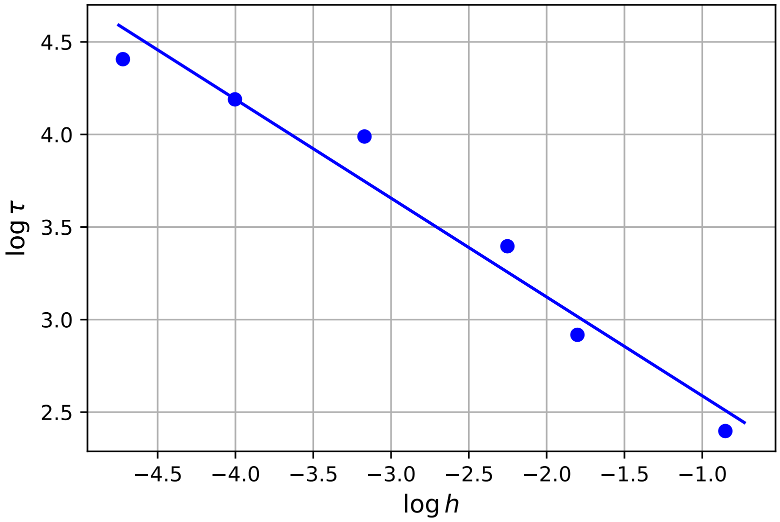

Figure 4.5: The characteristic time $\tau$ spent in the bottleneck region before a hysteresis jump with respect to different magnetic field strengths $h = \frac{H}{H_c} - 1$. The $\tau$ values are acquired from fitting (4.5) to the droplet elongation trajectories shown in Figure 4.4. The blue line is the linear fit with a slope of $k = -0.534$, closely matching the theoretically expected slope of $-0.5$ [15].

Figure 4.5 shows the numerically determined bottleneck behaviour of the droplet close to the critical field parameter $Bm_c$ before "jumping" over the instable region to a stable configuration. The $\tau$ values are acquired from fitting (4.5) to the droplet elongation trajectories shown in Figure 4.4. The time spent in the "bottleneck" is expected to follow [15]

$$\tau \sim \frac{1}{\sqrt{h}}, \tag{4.6}$$

where $h = \frac{H}{H_c} - 1 = \sqrt{\frac{Bm}{Bm_c}} - 1$, or $\log \tau \sim -0.5 \log h$ in logarithmic terms, which as shown in Fig. 4.5 is in good agreement with the value of $k = -0.534$ determined from the numerical simulations.

### 4.3.2 Virial method and Rayleigh's dissipation function approach

Investigation of the elongation of quasi-stable droplet dynamics permits us to explore the usefulness of another method used in theoretical description of magnetic fluid droplets which relies on the virial theorem [1, 13] and the Rayleigh dissipation function [69, 70].

The bottleneck neighbourhood has a stationary point of inflection of the droplet's energy, with respect to its eccentricity $\partial_e E = \partial_{ee}^2 E = 0$ [5]. This energy is the sum of the droplet's surface and magnetic energies.

The presence of this stationary inflection point allows for an approximation of the bottleneck dynamics around it in terms of unspecified constants [15]:

$$D\dot{e} = Ah + B(e - e_c)^2, \tag{4.7}$$

with the constants evaluated at the critical point $e = e_c$ and $H = H_c$:

$$D = -\eta R_0^3 f(e_c), \qquad A = H_c \frac{\partial^2 E}{\partial H \partial e}, \qquad B = \frac{1}{2}\frac{\partial^3 E}{\partial e^3}, \tag{4.8}$$

where $\eta$ is again the viscosity of the droplet viscosity and $f(e)$ is some unknown function of the droplet shape. This function will be determined using the virial method and the Rayleigh dissipation function.

Using the boundary conditions, it is now possible to express the constants of (4.7) explicitly, as shown in Appendix A.3:

$$D = \frac{8e_c}{9(1-e_c^2)^{1/2}}, \quad A = \frac{8\pi}{3}\, Bm_c\, \frac{6e_c + (e_c^2-3)\log\left[\frac{1+e_c}{1-e_c}\right]}{2e_c^4} \quad B = -\frac{1}{2}\frac{\partial^3 E}{\partial e^3}\frac{(1-e_c^2)^3}{e_c^2}.$$

We are able to compare the accuracy of these expressions to the values of the constants determined from the simulations. That is achieved by fitting the hyperbolic equation (4.5) to the numerical dynamics calculated around the bottleneck region, which provides the value of the constant $S = A/(2D)(H^2/H_c^2 - 1)$ [15]. Using a linear fit to the determined $S$ values versus the relevant $H^2$ values gives the slope that is an estimate of the $A/2D$ ratio.

Moreover, characteristic times spent in the bottleneck neighbourhood $\tau$ (Figure 4.5) can also be fit with the relation $\tau = \tau_0/\sqrt{h}$ [15] to obtain estimates of the capillary time $\tau_0 = \sqrt{AB}/D$.

The values of the constants found by the different approaches are shown in Table 4.1, where Bacri83 refers to the experimental results obtained in [15]:

| | Bacri83 | Virial th. | Numerical |
|---|---|---|---|
| $A\ /\ 2D$ | 0.73 | 1.18 | 0.98 |
| $\sqrt{AB}\ /\ D$ | 0.9 | 0.6 | 1.0 |

Table 4.1: Comparison of the determined values using various approaches.

## 4.4 Summary

This chapter shows multiple examples of the algorithm being validated with some theoretical relationships. The validation tests covered both purely hydrodynamical settings, as well as non-trivial magnetic phenomena as well. The algorithm is able to qualitatively capture the hysteresis behaviour of highly magnetic droplets, an effect previously unseen in three-dimensional and non-axisymmetric simulations. It is also able to quantitatively reproduce the critical exponents of the instability bifurcations.

All these tests hint at the algorithm being able to stand on its own and possibly being useful in exploring situations where no theoretical relations exist at the time of writing this thesis. We will explore these cases in the next chapter.

# Chapter 5

# Simulations

## Contents

This chapter surveys the various simulations performed by the newly developed algorithm that, to our best knowledge, have not been done before. Multiple simulations were performed both in constant and rotating magnetic fields to better explore the applicability and limits of the algorithm.

The simulations of a droplet in a constant field yield two important results. First, the algorithm is able to capture the conical tip development of highly magnetic droplets, as has been predicted [30, 71] previously with droplets of strong dielectric and magnetic properties.

And second, the simulated droplet shapes in increasing magnetic field strengths once the droplets have equilibriated are comparable with the shape evolution that has been observed experimentally. This comparability with experimental results allows for indirect inference of droplet parameters like viscosity, permeability and surface tension, which has previously been rather difficult for microscopic magnetic fluid droplets. This inference can be performed by fitting the simulation parameters so that the calculated evolution most closely matches the experimentally observed evolution. However, this approach is more a proof of concept rather than a practically usable approach, as the simulations take a prohibitively long time.

In the case of a rotating field, three notable results have been achieved. First, back-and-forth motion of a liquid object – magnetic fluid droplet – has been simulated in three dimensions. This effect has been previously observed in solid magnetic rods and elastic magnetic filaments.

Second, the development of the starfish instability has been numerically captured and the critical field at which this instability arises has been determined from the droplet shape evolution as well.

Finally, the simulations qualitatively point to a re-entrant transition whereby a droplet that has undergone an oblate-prolate transition in increasing magnetic field strengths will revert back to an oblate shape in even higher fields.

## 5.1 Constant field

### 5.1.1 Conical tip development

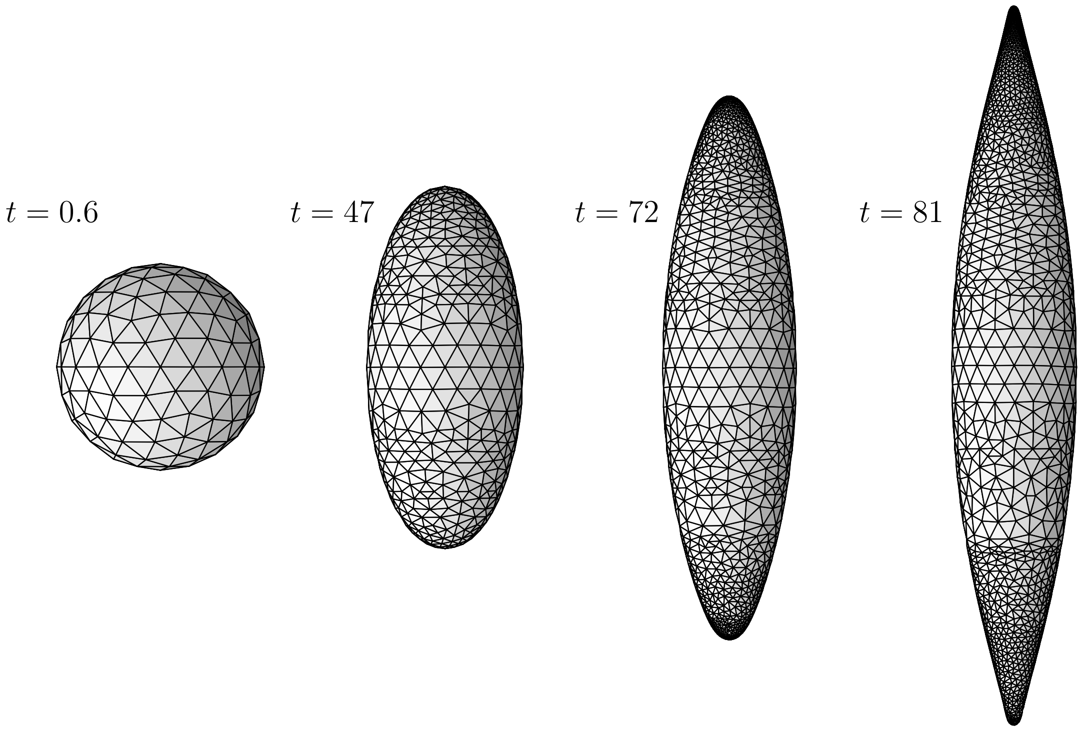

Figure 5.1: Droplet elongation in a constant magnetic field with $Bm = 5$, $\mu = 30$, $\lambda = 10$. Development of sharp tips can be seen, as well as addition of nodes in regions of high surface curvature. This simulation was halted at $t = 80.96$ before it had reached an equilibrium, as the droplet had developed prohibitively many points near its tips. This figure has been obtained in collaboration with A. P. Stikuts.

An initially spherical magnetic fluid droplet is subjected to a constant homogeneous magnetic field and it stretches at a some rate until it reaches an equilibrium elongation, where the magnetic forces balance the surface tension force. For droplets of high magnetic permeability $\mu$ at high enough magnetic fields, it is possible for them to even grow sharp conical tips. A similar effect has been predicted [30] and observed [5] before. Here we are able to recapture this phenomenon numerically, as shown by simulation results in Figure 5.1.

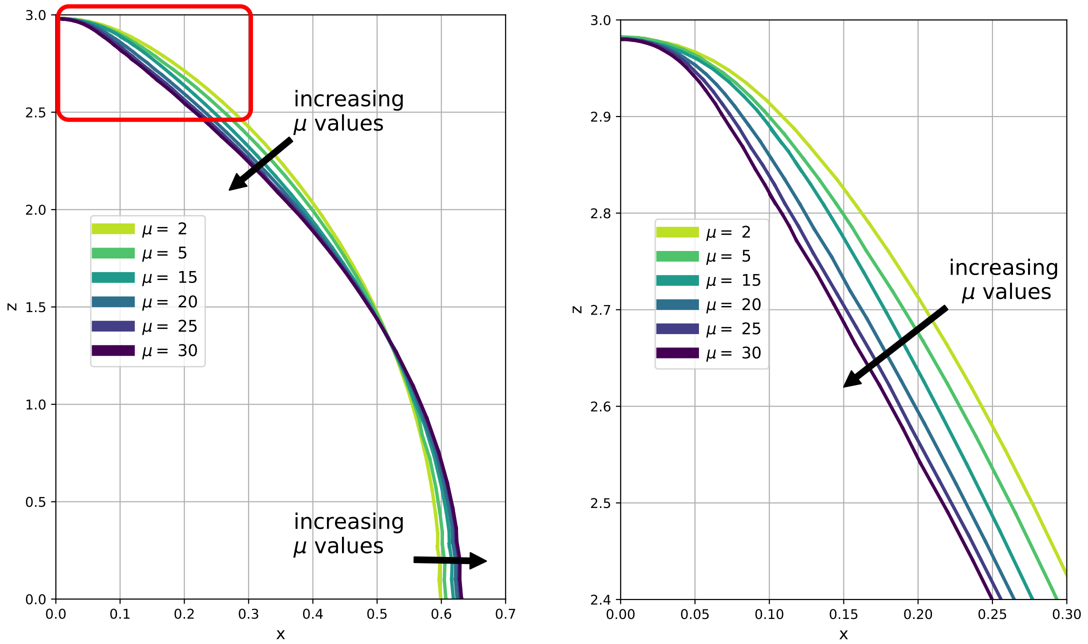

Figure 5.2: Droplet shape outlines during elongation at different $\mu$ values in a constant magnetic field, acquired via projection of the complete three-dimensional simulation in a plane. All elongation simulations were performed in a magnetic field that for the particular value would yield an equilibrium elongation axis ratio of $a/b = 13$. The plot displays a snapshot of the moment the droplet tips stretched to $z = 3$. Larger values of $\mu$ seem to be developing sharper tips even before attaining the equilibrium. The $x, z$ axes have been scaled to highlight the outline differences. The right figure shows a zoomed-in red region of the left figure around the droplet tips.

The Figure 5.2 shows qualitatively distinct behaviour when droplets elongate in a constant magnetic field for different values of magnetic permeability $\mu$. This particular range of $\mu$ values was explored, as it includes the critical value of $\mu_c \simeq 21$ at which hysteresis becomes possible. At larger values of $\mu$ during the stretching of the droplet, it may develop sharp cone-like tips, a phenomenon not observed at smaller $\mu$ values [30].

This effect of conical tip development has been observed before in axi-symmetric two-dimensional simulations [31].

### 5.1.2 Comparison with droplet elongation in experiments

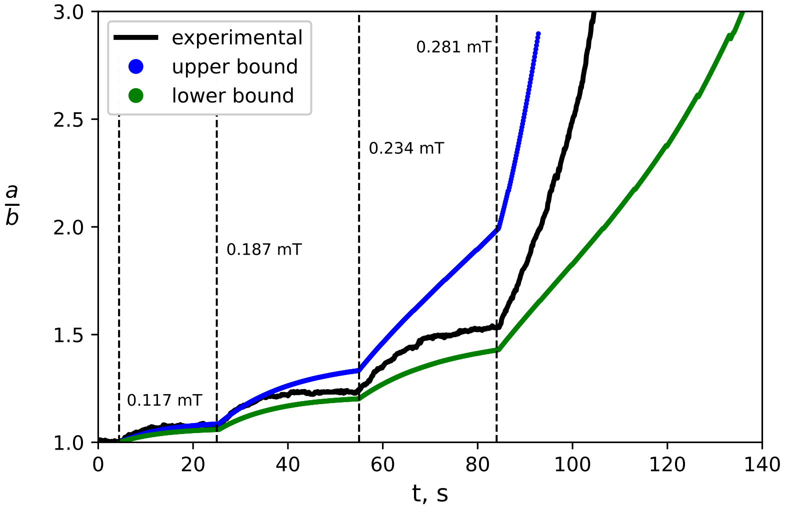

Figure 5.3: Stretching of a magnetic fluid droplet in a magnetic field, increasing from zero in a stepwise manner, indicated by the dotted lines. In black – experimental results with $\mu = 34 \pm 1.5$, $\gamma = (8.2 \pm 0.4) \cdot 10^{-7} J/m^2$, $\lambda = 10.1 \pm 2.5$) in an external magnetic field. The blue and green curves are obtained numerically with ($\mu = 34$, $\gamma = 7.7 \cdot 10^{-7} J/m^2$, $\lambda = 7.6$) and ($\mu = 34$, $\gamma = 8.2 \cdot 10^{-7} J/m^2$, $\lambda = 7.6$), respectively. The numerically calculated curves allow to indirectly find the bounds of the droplet parameter values. Experimental data supplied by A.P. Stikuts.

This algorithm allows to capture of the droplet stretching rate. An example of a magnetic fluid droplet elongation measured experimentally is shown in Figure 5.3, where an initially spherical droplet is subjected to homogeneous magnetic fields of increasing magnitude. The fields strengths start at zero and are increased in a stepwise manner once the droplet elongation has equilibriated. The procedure of this experiment follows the protocol explained in [43] and the parameters of the droplet are shown in Figure 5.3. Variation of droplet parameters allows us to best match the simulation results to the experimentally observed results. This approach is able to produce parameter bounds, so that their corresponding simulation results enclose the experimental elongation curve from below and above – this would indirectly hint at the underlying bounds of droplet parameters like their surface tension $\gamma$, magnetic permeability $\mu$ and the ratio of viscosities $\lambda$. Estimating these parameters is usually a challenge for microscopic droplets.

Nonetheless, we should mention that these calculations require large computational resources and since there are three parameters to be estimated, this approach of droplet parameter estimation does not seem practical at the moment.

A step towards application in practice, however, might be observing only slightly deformed droplet elongation–relaxation, where the simulations would require less nodes to describe the droplet shape accurately.

## 5.2 Rotating field

### 5.2.1 Back–and–forth motion

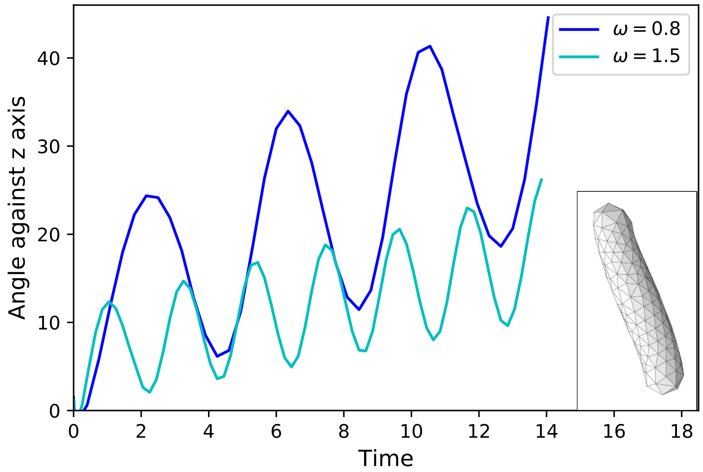

Figure 5.4: Back–and–forth motion of a droplet (shown in the inset), that has been first elongated in a constant magnetic field, in moderately fast rotating fields of different dimensionless frequencies $\omega$. The curves represent the angle between longest droplet axis and the stationary $z$ axis. Parameters used in simulations: $\mu = 30$, $Bm = 10$, $\lambda = 1$. Here node addition was disabled, to speed up the simulations.

Another phenomenon of droplet behaviour in a rotating field was explored. Droplets that were initially elongated in a constant field were then exposed to a rotating magnetic field of various dimensionless frequencies $\omega$.

At small rotation frequencies, the droplet follows the external magnetic field, as expected. However, at larger frequencies, a back-and-forth motion of the liquid droplet was observed, as seen in Figure 5.4 where the angle of the longest droplet axis is shown to be oscillating around an averaged uniform rotation with respect to the $z$ axis. There are hints of rotational modes being present as well, as indicated by the almost perfect matching up of the two evolution curves of the rotational frequencies that are almost a multiple of one another.

Similar effects have been observed with solid elongated paramagnetic particles [72], self–propelling magnetic particles [73], as well as magnetotactic bacteria [74]. To our knowledge, liquid particle back-and-forth motion has not been previously simulated.

These simulations did not employ the node addition stabilization technique, as the accurate description of such really deformed droplets would require too many mesh nodes. All the other mesh stabilization algorithms were still used. Therefore these results are qualitative.

### 5.2.2 The “starfish” instability

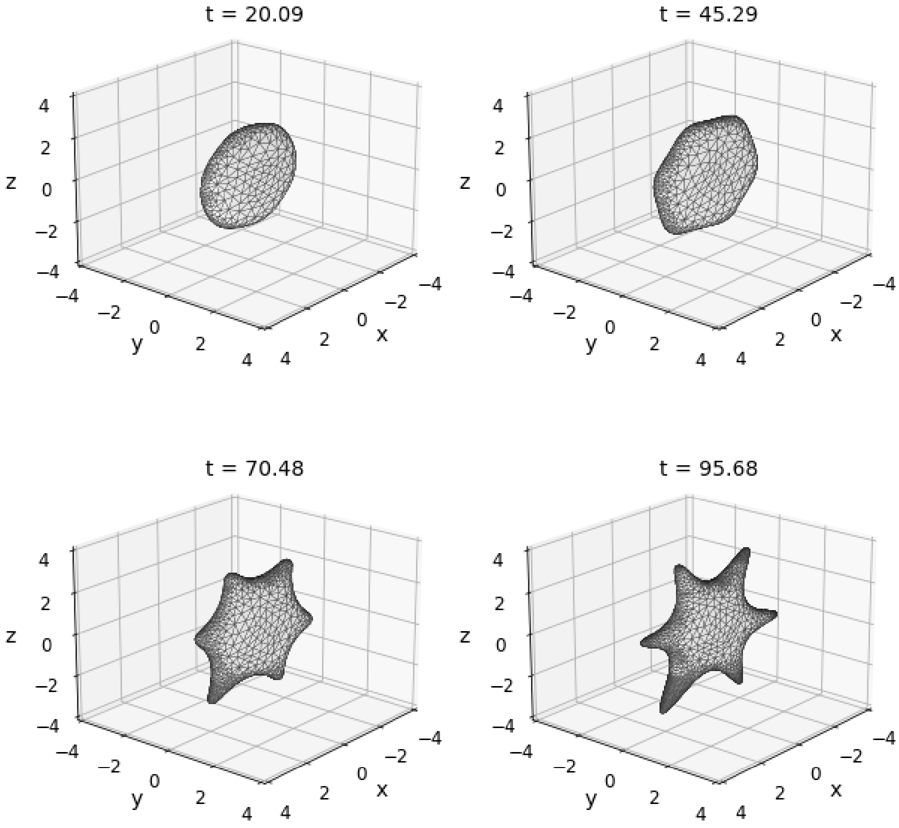

Figure 5.5: Example of the starfish instability developing in a rotating magnetic field, using $Bm = 35,\ \mu = 10,\ \omega = 10,\ \lambda = 7.6$ and the node addition cut-off criteria of 0.4.

The algorithm gives us the ability to explore the beginning of the starfish instability, exemplified in Figure 5.5. It is known to occur at fast enough and strong enough rotating magnetic fields, when the oblate magnetic fluid droplet “grows” finger–like structures around its perimeter [7].

We also managed to observe competition of these instability modes (arrangements of a different number of these “fingers”), as can be seen in Figure 5.6 where at the beginning the droplet seems to growing the mode of $n = 6$ which is eventually beat by the very pronounced $n = 4$ mode.

These instability “fingers” seem to have arisen from some mesh asymmetries, that may arise during the stabilization of the mesh, whereby one region of the surface might have new nodes added to it or some edge flips happen there, while another region might have avoided such maintenance.

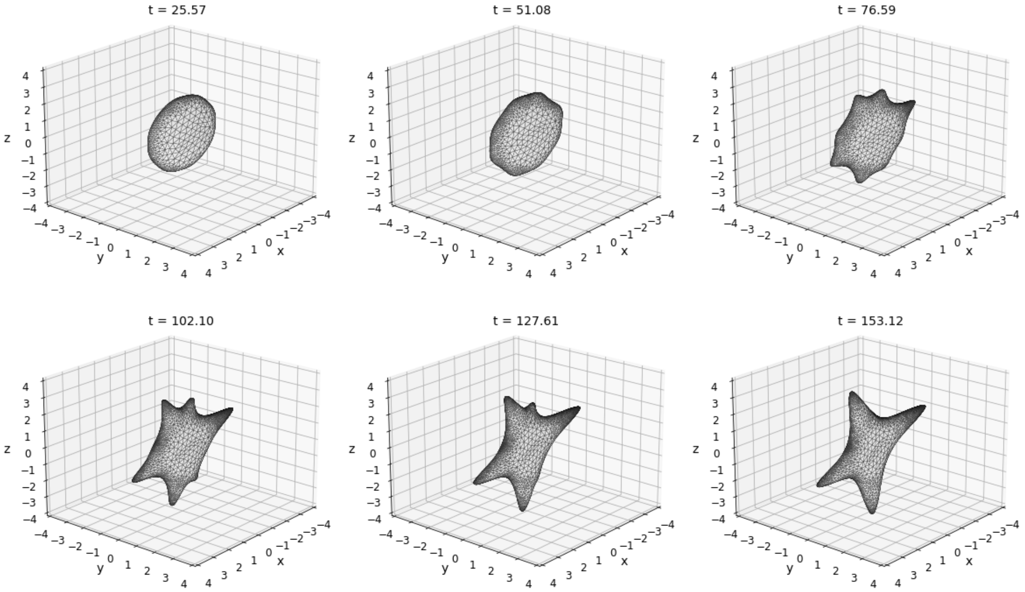

Figure 5.6: Starfish instability mode competition using $Bm = 30$, $\mu = 10$, $\omega = 10$, $\lambda = 7.6$ and the node addition cut-off criteria of 0.4. Initially, the $n = 6$ mode seems to be developing, but eventually only the $n = 4$ mode has remained.

#### 5.2.2.1 Field threshold determination

In order to thoroughly investigate the nature of the onset and evolution of these modes, we performed the following procedure. Initially, we start with an axially symmetric oblate ellipsoid, the axis ratios of which have been calculated to correspond to a minimal energy shape in an infinitely fast rotating magnetic field [7, 8]. Then, a tiny sinusoidal perturbation, with its period corresponding to the particular mode $n$, is added along the perimeter of the droplet in the plane of rotating field:

$$\delta r(\theta) = \varepsilon \cos(\omega_n \theta), \tag{5.1}$$

where $\varepsilon = 0.01$ is an arbitrary number to make the perturbation small and $\omega_n$ scales the perturbation profile to create the desired number of instability "fingers". We apply this perturbation in the plane of rotation of the magnetic field (here the $XZ$ plane) to the position of every node $i$:

$$x^{(i)} = x_0^{(i)} + \delta r \cdot \cos\theta^{(i)} \cdot r^{(i)}, \tag{5.2}$$

$$z^{(i)} = z_0^{(i)} + \delta r \cdot \sin\theta^{(i)} \cdot r^{(i)}, \tag{5.3}$$

where the zero subscript indicates the unperturbed coordinate, $\theta^{(i)}$ is the angle the $i$-th node makes with the $x$ axis after being projected into the $XZ$ plane and $r^{(i)}$ is its distance to the origin in this plane. After this perturbation is applied, the droplet volume is rescaled and it is then evolved in a period-averaged high frequency magnetic field of various strengths. This approach allows us to explore whether each mode would grow or decay at the particular field strength.

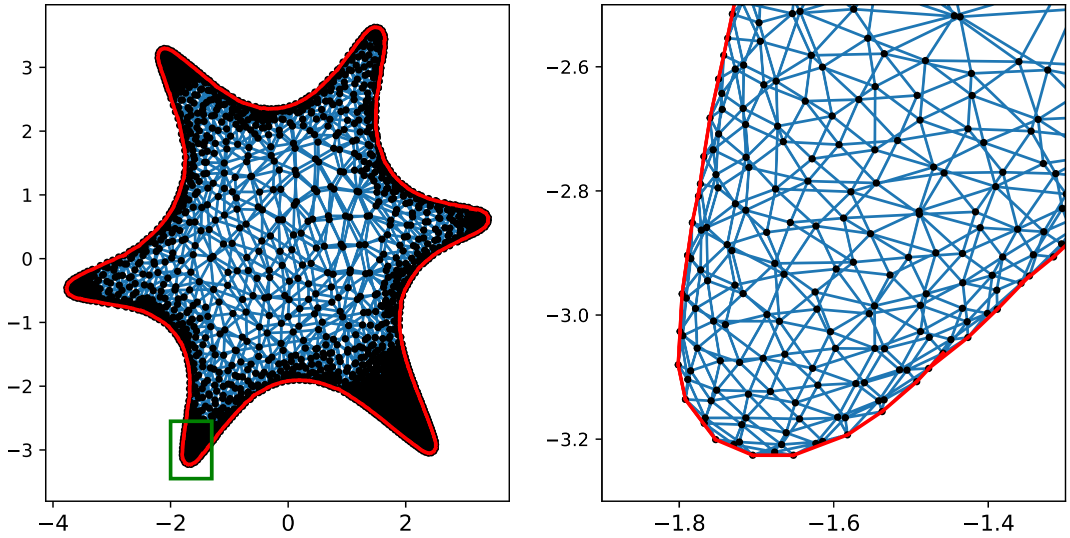

Figure 5.7: The droplet mesh is projected onto to the plane of the rotating magnetic field in order to find its hull (red). The figure on the right shows a zoomed in region of one of the six starfish "fingers", bounded by the green square in the left figure.

To tackle this problem quantitatively, we need to project the droplet mesh onto the plane of rotating field, where we can then find the outline (hull) of the droplet perimeter, as shown in Figure 5.7. Once that is done, it is possible to "unroll" the hull in terms of plane polar coordinates $r(\theta)$ on which it is then easy to apply Fourier mode analysis.

Since the droplet is perturbed near its equilibrium, linear response of the perturbation can be assumed $\dot{\varepsilon} = \beta\varepsilon$, and with it, an exponential evolution of the perturbation $\varepsilon(t) \propto e^{\beta t}$, where $\beta$ is the so called logarithmic increment. In further analysis, we consider the pertinent Fourier mode $A_n$ to represent the surface perturbation $\varepsilon = A_n$ and $\beta_n$ to represent its corresponding logarithmic increment. An example of this exponential Fourier amplitude evolution is shown in Figure 5.8.

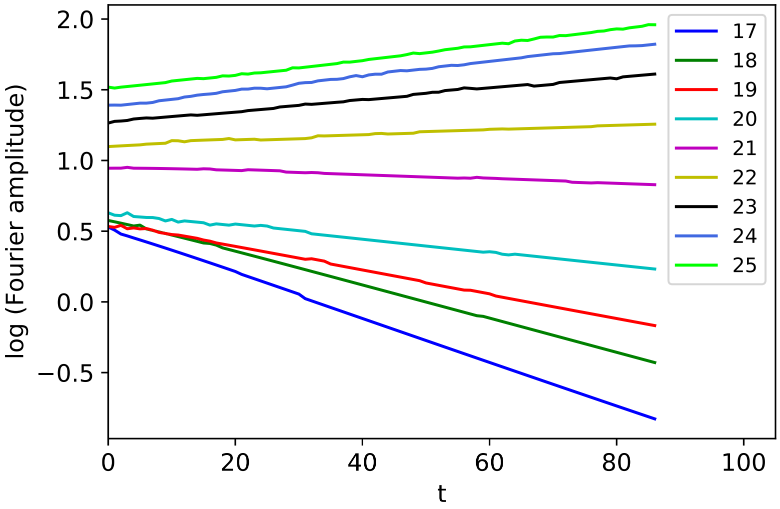

Figure 5.8: Evolution of logarithm of the Fourier mode $A_3$ at various magnetic field strengths, $\mu = 10$. Two things can be observed: the amplitude evolution is exponential, as expected from the linear response assumption, here evidenced by the straight lines; and the slope of curves, represented by $\beta_3$, changes from negative to positive with increasing magnetic fields, indicating a critical field, above which the perturbation no longer decays. In this case of the $n = 3$ mode, we find this critical field to be $21 \leq Bm_c \leq 22$.

This Fourier amplitude analysis can be used to determine the value of the critical magnetic at which a certain mode would develop. To determine this critical field $Bm_c$, one has to find the magnetic field value at which the slope (logarithmic increment) $\beta$ of the log-amplitude evolution (shown in Figure 5.8) changes sign. A particular example of this $\beta$ sign change is shown in Figure 5.9 in the case of $\beta_3$, as obtained from the evolution curves in Figure 5.8.

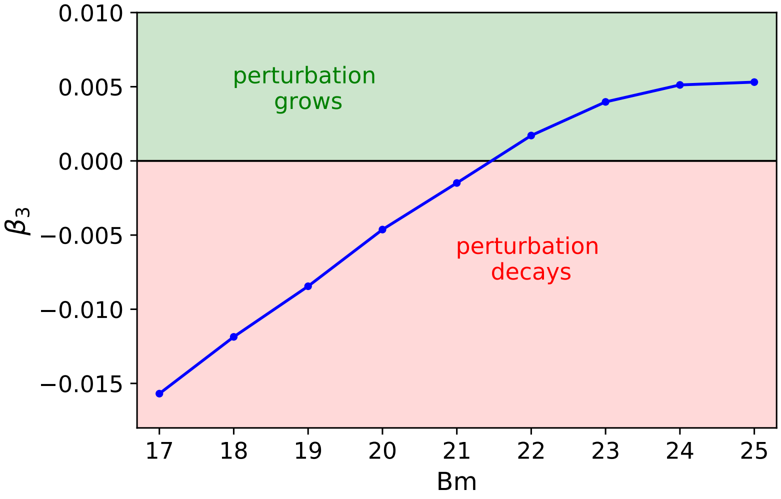

Figure 5.9: Logarithmic increment $\beta_3$ at various field values, obtained from analysis of Figure 5.8. The sign change indicates a critical field, above which the perturbation no longer decays. In this case of the $n = 3$ mode, we find this critical field to be $21 \leq Bm_c \leq 22$.

A particularly interesting mode to investigate is the $n = 2$ mode, whose growth would indicate the oblate-prolate transition, or, in possibly more relatable terms, pancake-like shape to rugby-ball-like shape transition.

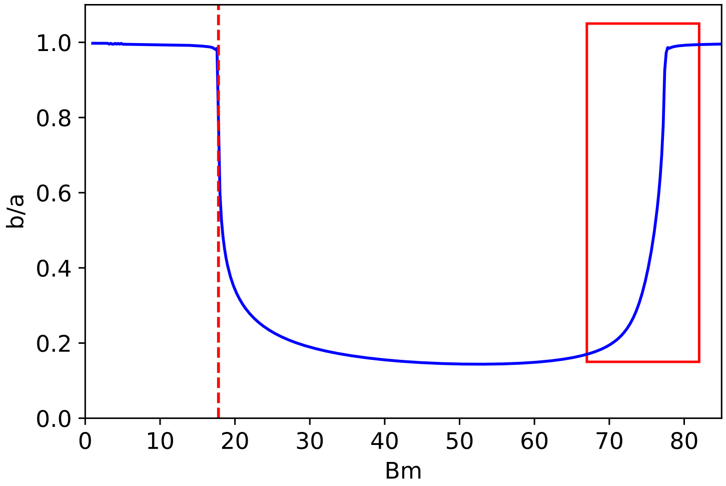

Figure 5.10: The vertical red line on the left side of figure shows the critical field determined via the logarithmic increment $\beta_2$ changing sign. It matches perfectly with the value calculated via droplet energy minimization (blue). The square area on the right side of the figure shows the droplet becoming oblate (pancake-like) again at larger magnetic fields. Simulated using $\mu = 10$.

This transition is indicated by the sharp drop of the blue curve in Figure 5.10. The blue curve been calculated numerically by minimizing the energy of a droplet, presumed to be ellipsoidal [8, 43]. The critical field of the transition found by analyzing the behaviour of $\beta_2$ with increasing magnetic fields (shown in dashed red in Figure 5.10) matches very closely to the energy minimization prediction.

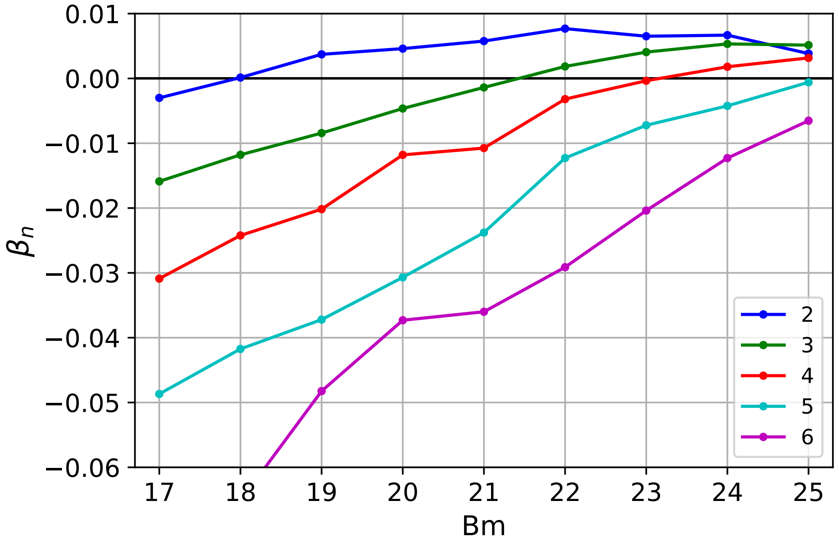

Figure 5.11: Logarithmic increments $\beta_n$ of various instability "finger" modes at different magnetic fields $Bm$. Mode competition can be noticed as the $\beta_n$'s close in on one another at larger magnetic fields. Simulated using $\mu = 10$.

Figure 5.11 displays a multitude of $\beta_n$ values and their behaviour with increasing magnetic fields, there are multiple things to deduce from this figure. First, the $\beta$ values seem to be increasing with larger magnetic fields, however, $\beta_2$ seems to have peaked at $Bm = 22$. This non-monotonicity will be explored shortly. Second, the ordering of the critical fields seems to be consistent – larger critical fields for larger modes. Third, at larger magnetic fields we can observe the relative order of the $\beta$'s changing: at $Bm = 25$ the $\beta_2$ becomes smaller than $\beta_3$, indicating a kind of competition between modes we have observed previously in Figure 5.6. It is not evident that the mode $n = 3$ would overtake the mode $n = 2$ at $Bm = 25$, if the $n = 2$ mode had already established itself. However, starting from small random perturbation along a spherical droplet surface at $Bm = 25$ the $n = 3$ mode would probably emerge as the dominant one.

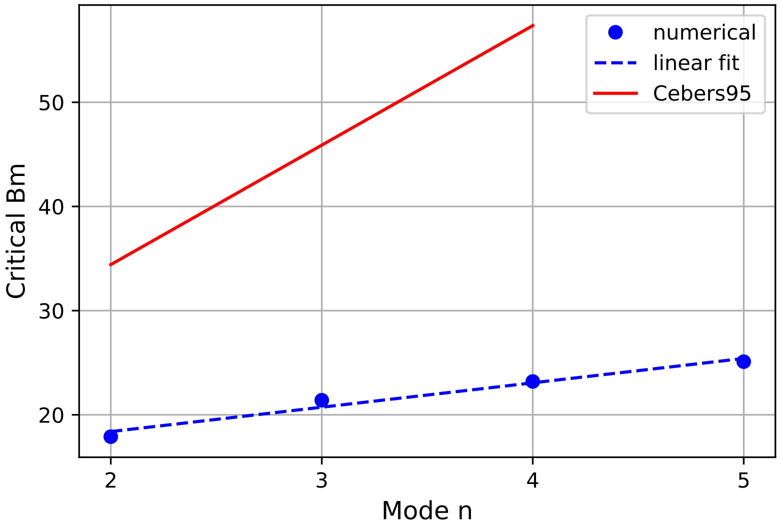

Figure 5.12: "Starfish" instability modes $n$ and their corresponding minimal critical magnetic fields $Bm_c$ above which they could manifest themselves, at $\mu = 10$. However, having the field above this threshold value is not sufficient to observe the particular mode, as other modes might be more pronounced. Comparison with the theoretical prediction [75] in red. Both results show a linear relationship. The high theoretical $Bm_c$ estimates (red) might be explained by an underestimate of capillary effects.

Looking at the critical magnetic fields as determined by analysing the $\beta_n$ sign changes in Figure 5.11, we can display their evolution with respect to their mode number $n$, as shown in Figure 5.12.

The linear relationship of increasing critical fields with mode number corroborates the theoretical predictions of Cēbers et al. [75], made under the assumption of an infinitely long cylindrical magnetic fluid droplet, shown with a solid red line in Figure 5.12. This linear relation has also been observed experimentally [7].

The theoretical overestimate of the critical $Bm$ value might be explained by the assumption of the infinitely long cylinder. In such a case, the principal curvature describing the deformation along the long axis of the cylinder is identically zero, thus lowering the effective capillary force $\gamma(k_1 + k_2)$ due to surface tension, where $k_1, k_2$ are the principal curvatures of the surface. In three dimensions both of the principal curvatures would be nonzero around a surface instability. Since the Bond magnetic number $Bm$ represents the ratio of magnetic to capillary forces, an underestimate of the latter would overestimate the critical $Bm$ value.

### 5.2.3 Re-entrant transition

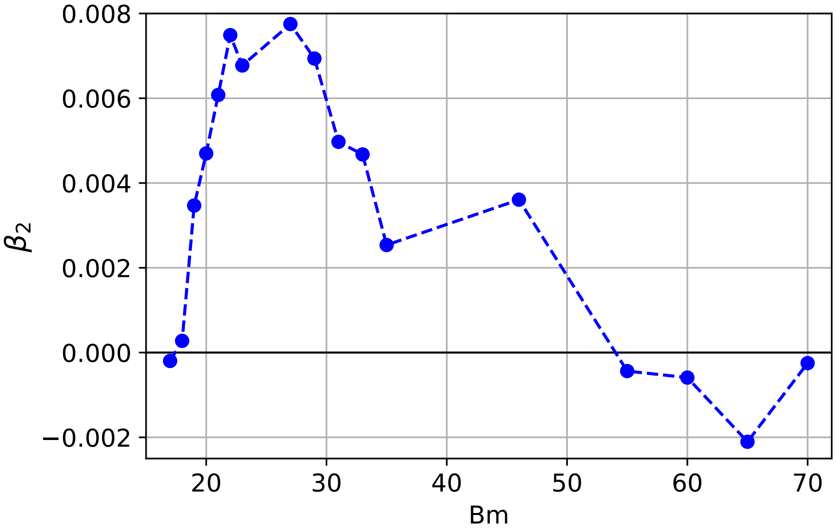

Figure 5.13: The logarithmic increment of the starfish mode $n = 2$ of a droplet with $\mu = 10$ becomes positive at $Bm \approx 18$, indicating a transition to a prolate shape, which can be reversed at large fields, when the droplet becomes oblate again – this reentrant transition was predicted and observed in [7].

The droplet energy minimization approach [8, 43] shown in blue in Figure 5.10, as well as experimental observations [7] at large enough magnetic fields ($Bm \gtrsim 70$)

predict the droplet undergoing a prolate-oblate transition – reverting back to its pancake-like shape seen previously at lower magnetic fields.

We observe a qualitatively similar result in the analysis of Fourier modes $A_2$ of slightly perturbed ellipsoidal droplets, where in stronger magnetic fields $Bm \gtrsim 50$ the growth increment $\beta_2$ becomes negative again, indicating the decay of the $n = 2$ mode and thus allowing the droplet to re-enter its oblate form again.

There seems to be a discrepancy in the prediction of the critical field values of the re-entrant transition between the energy minimization approach and our numerical perturbation analysis. This difference might have hint at the limits of the ellipsoidal approximation used in deriving the critical field in the energy minimization approach. However, in order to increase confidence in the numerical result, we would need to begin our perturbation analysis from the prolate shape, rather than indirectly predicting it from the perturbation behaviour of the oblate droplet shape.

# Chapter 6

# Conclusion

## Contents

## 6.1 Discussion

The development of the boundary element method algorithm for three-dimensional magnetic fluid free interface dynamics allows to validate various relations describing their behavior and may be compared with experimental data, thus providing insight regarding the physical properties of the concentrated phase of magnetic colloids. These colloids can have many interesting properties due to their highly magnetic nature – such as dependence of rheological properties or surface tension on the magnetic field.

The newly created numerical tool has been tested against some theoretical solutions where possible – equilibrium curves of droplet elongation in constant magnetic fields with various relative magnetic permeability $\mu$ values, the exponential decay of small elongations under surface tension without external magnetic fields, the dynamical behaviour around the hysteresis bottleneck instability regions, as well as droplet dynamics in various rotating field configurations and the critical fields for oblate–prolate transition. These tests allow to probe the limits of various theoretical approximations and assumptions often used in description of magnetic fluid droplets, for a notable example, the assumption of ellipsoidal shape.

The correspondence of theoretical predictions with numerical results also extends the application limits of the simple magnetic fluid model description of these droplets, which seem to be a rather new kind of soft magnetic matter with *a priori* nontrivial physical properties.

The algorithm has also been shown to be appropriate in prediction of full three-dimensional droplet dynamics with arbitrary droplet-fluid viscosity ratios in uniform fields, both static and rotating up to moderately large droplet deformations. This is important, as experimentally magnetic fluid droplets are not usually axisymmetric and so have to be described carefully in 3D, and can reach viscosity ratios of $\lambda \approx 100$. The algorithm also allows to explore droplet dynamics in rotating magnetic fields of moderate frequencies, where the fast–rotating field averaging approximation does not hold, which has not been previously possible.

In addition, the algorithm can capture the expected characteristic behaviour of magnetic fluid droplets in rotating magnetic fields, in particular, following the external field at low rotation frequencies and exhibiting a back-and-forth motion at moderately fast fields, similarly to solid magnetic rods or particles, as well as the droplet undergoing the oblate–prolate–oblate transition at fast rotating fields of increasing strength.

However, the algorithm is currently limited in its ability to simulate large deformations of the droplet. It also is unable to simulate a symmetrical appearance of the starfish instability modes without an artificial perturbation of the droplet's shape. The unperturbed starfish instability modes possessed a certain asymmetry both in their angular position and their length as well. In order to speed up the simulation times, the node removal routine in regions of small surface curvature should be implemented, as has been demonstrated previously [36]. Moreover, the existing algorithm version relies on assumptions of uniform surface tension and linear magnetization of the droplet. And finally, the present algorithm cannot handle topological changes of droplets like coalescence or breakup, as well as multiple drops interacting. It is, however, possible to extend the BEM algorithm to these cases[35].

A notable contribution of this work is the numerical confirmation of the main characteristics of magnetic fluid droplet behavior in static and rotating fields. This allows for the study of droplet dynamics in highly non–equilibrium situations not tractable at present by any theoretical approach, as well as exploring various phenomena that may be sensitive to the precise values of multiple physical parameters of either the droplet or its surroundings.

## 6.2 Main conclusions

- When the "starfish" instability modes of a droplet in a rotating field compete, the mode appearing first may not turn out to be the dominant one.
- Analysis of droplet surface perturbation evolution allows to precisely determine the magnetic field thresholds above which the manisfestation of particular "starfish" instability modes is possible.
- Higher "starfish" instability modes require stronger magnetic fields to appear.
- Fluid magnetic objects can exhibit back-and-forth motion in rotating magnetic

fields, similarly to their solid counterparts.

- The model of an infinitely long cylindrical magnetic fluid droplet [75] overestimates the critical field at which the "starfish" instability occurs, possibly due to an underestimate of the capillary forces.
- The simple model of a magnetic fluid droplet is sufficient to capture the various complex surface dynamics of the droplet in external fields, in spite of the additional assumptions of linear magnetic susceptibility and uniform surface tension.

## 6.3 Thesis

Using simulations of boundary integral equations it is possible to fully describe the three-dimensional free interface dynamics of magnetic fluid droplets.

# Appendix A

# Derivations

## A.1 Normal field calculation without the tangential components

Adapting the approach taken in [42] we have an integral equation of the normal differences on the droplet surface

$$[\![H_n(\boldsymbol{y})]\!]\left(\frac{\mu}{\mu-1}-L(\boldsymbol{y})\right)=H_{0n}(\boldsymbol{y})-\int_S\left([\![H_n(\boldsymbol{x})]\!]-[\![H_n(\boldsymbol{y})]\!]\right)\boldsymbol{n}(\boldsymbol{y})\cdot\boldsymbol{\nabla}_y\frac{1}{4\pi r}dS_x, \tag{A.1}$$

where $[\![H_n(\boldsymbol{y})]\!]=H_n^{(e)}(\boldsymbol{y})-H_n^{(i)}(\boldsymbol{y})$, and we have

$$H_n^{(e)}=\frac{[\![H_n]\!]}{\mu-1}\mu \tag{A.2}$$

$$H_n^{(i)}=\frac{[\![H_n]\!]}{\mu-1}. \tag{A.3}$$

The function $L(\boldsymbol{y})$ is determined solely by the shape of the droplet [76]

$$L(\boldsymbol{y})=\frac{\boldsymbol{n}(\boldsymbol{y})}{4\pi}\cdot\int_S\left\{\left[\boldsymbol{n}(\boldsymbol{x})\cdot\boldsymbol{\nabla}\left(\frac{1}{r}\right)\right]\left[\boldsymbol{n}(\boldsymbol{y})-\boldsymbol{n}(\boldsymbol{x})\right]+\frac{\boldsymbol{\nabla}\cdot\boldsymbol{n}(\boldsymbol{x})}{r}\,\boldsymbol{n}(\boldsymbol{x})\right\}dS_x. \tag{A.4}$$

## A.2 Magnetic field tangential component

We begin with an equation from [42] where we put the magnetic field $\boldsymbol{H}$ in place of the electric field $\boldsymbol{E}$:

$$\boldsymbol{H}(\boldsymbol{y}) = \boldsymbol{H_0}(\boldsymbol{y}) - \int_S [\![H_n(\boldsymbol{x})]\!] \boldsymbol{\nabla}_y \frac{1}{4\pi r} \mathrm{d}S_x - \frac{1}{2}[\![H_n(\boldsymbol{x})]\!]\boldsymbol{n}(\boldsymbol{y}). \tag{A.5}$$

To extract the tangential component, we apply a cross product with $\boldsymbol{n}(\boldsymbol{y})$:

$$\boldsymbol{n}(\boldsymbol{y}) \times \boldsymbol{H_t}(\boldsymbol{y}) = \boldsymbol{n}(\boldsymbol{y}) \times \boldsymbol{H_0}(\boldsymbol{y}) + \frac{1}{4\pi}\int_S [\![H_n(\boldsymbol{x})]\!](\boldsymbol{n}(\boldsymbol{y}) \times \boldsymbol{r})\frac{\mathrm{d}S_x}{r^3} \tag{A.6}$$

where we note that only the tangential component of the field give a contribution to the cross product.

However, this integrand is strongly singular as $\boldsymbol{x} \to \boldsymbol{y}$, the it scales as $O(1/r^2)$

Nonetheless, we can regularize this equation by multiplying $[\![H_n(\boldsymbol{y})]\!]$ with the identity

$$\int_S \frac{\boldsymbol{n}(\boldsymbol{x}) \times \boldsymbol{r}}{4\pi r^3}\mathrm{d}S_x = \int_V \boldsymbol{\nabla} \times \left(\frac{\vec{r}}{4\pi r^3}\right)\mathrm{d}V = \int_V \boldsymbol{\nabla} \times \left(\boldsymbol{\nabla}\frac{1}{4\pi r}\right)\mathrm{d}V = 0 \tag{A.7}$$

and subtracting it from (A.6) to arrive at

$$\boldsymbol{n}(\boldsymbol{y}) \times \boldsymbol{H_t}(\boldsymbol{y}) = \boldsymbol{n}(\boldsymbol{y}) \times \boldsymbol{H_0}(\boldsymbol{y}) + \frac{1}{4\pi}\int_S \frac{\mathrm{d}S_x}{r^3}\left(\left[[\![H_n(\boldsymbol{x})]\!]\boldsymbol{n}(\boldsymbol{y}) - [\![H_n(\boldsymbol{y})]\!]\boldsymbol{n}(\boldsymbol{x})\right] \times \boldsymbol{r}\right) \tag{A.8}$$

This integrand now scales as $O(1/r)$ as $\boldsymbol{x} \to \boldsymbol{y}$ and can now be tackled using, for example, local polar coordinates as we have seen before.

The left hand side of (A.8) simplifies to $H_t(\boldsymbol{y})$, as the normal is of unit length and is at a a right angle with the tangential component. Therefore, we are able to obtain the magnitude of tangential component of the magnetic field. This procedure is more numerically stable than the method of numerical differentiation of the magnetic potential $\psi$ on the droplet surface outlined in the main text.

## A.3 The virial theorem approach

The dynamics of the droplet in the neighbourhood of the “hysteresis jump” can be described by the Rayleigh dissipation function $R$ the change of the total droplet energy is expressed by $dE/dt = -2R$ and $R$ is given as a quadratic function in terms of the generalized velocity of the system – in this case $de/dt$ or $d(a/b)/dt$:

$$R = \frac{D\dot{e}^2}{2}. \tag{A.9}$$

Merging the above relations in an Euler–Lagrange equation gives

$$\frac{\partial E}{\partial e} = -D\dot{e}. \tag{A.10}$$

Around the threshold of the instability $\partial_e E = \partial_{ee}^2 E = 0$ the energy derivative can be expressed as

$$\frac{\partial E}{\partial e} \simeq \frac{1}{2}\frac{\partial^3 E}{\partial e^3}(e-e_c)^2 + H_c\,\frac{\partial^2 E}{\partial e \partial H}\,\frac{H-H_c}{H_c}, \tag{A.11}$$

or, making use of the constants $A, B, D$:

$$D\dot{e} = Ah + B(e-e_c)^2. \tag{A.12}$$

As the viscosity of the surrounding liquid is much smaller than that of the magnetic droplet, it can be ignored.

In that case the force balance on the droplet surface becomes

$$-p + \sigma_{nn}^v = -\gamma\left(\frac{1}{R_1} + \frac{1}{R_2}\right) + \frac{\mu_0}{2}M_n^2, \tag{A.13}$$

where $\sigma^v$ is the viscous stress tensor and $M$ is the magnetization. Assuming an ellipsoidal shape of the droplet, the equation of motion of the magnetic fluid reads

$$-\partial_i p + \partial_m \sigma_{im}^v = 0. \tag{A.14}$$

Multiplying (A.14) by $x_k$ and integrating it over the droplet volume, and relying on the boundary condition (A.13), we arrive at the virial coefficients

$$V_{ik} = \delta_{ik}\int pdV - \int \gamma x_k n_i\ \nabla\cdot\vec{n}\ dS + \int x_k n_k \frac{\mu_0}{2}M_n^2 dS - \int \sigma^v_{ik} dV = 0 \tag{A.15}$$

With help of $\int x_k n_i\ \nabla\cdot\vec{n}\ dS = -\int(\delta_{ik} - n_i n_k)\ dS$ as well as other relations [13] it can be shown that $V_{33} - \frac{1}{2}(V_{11}+V_{22}) = 0$ may be recast as

$$\begin{aligned} &-\int\left[\sigma^v_{33} - \frac{1}{2}(\sigma^v_{11}+\sigma^v_{22})\right]dV+ \\ &+2\pi\gamma R_0^2\left\{\frac{\mu_0}{2}Bm\left[\frac{(1-e^2)}{2}\left(\frac{(3-e^2)}{e^5}\log\left(\frac{1+e}{1-e}\right)-\frac{6}{e^4}\right)\right]+\right. \\ &\left.+\frac{\frac{(3-4e^2)\arcsin e}{e^3} - \frac{(3-2e^2)(1-e^2)^{1/2}}{e^2}}{2(1-e^2)^{1/6}}\right\} = 0, \end{aligned} \tag{A.16}$$

where we note that $Bm$ here is $\frac{M^2R_0}{\gamma}$ rather than the usual $\frac{H^2R_0}{\gamma}$.

Making use of the fact that droplet energy can be found by

$$E = -\frac{1}{2}\ \frac{\chi H^2}{1+\chi N/4\pi}\ \frac{R_0^3}{3} + \frac{2\pi\gamma R_0^2}{(1-e^2)^{1/6}}\left[\frac{\arcsin e}{e} + (1-e^2)^{1/2}\right], \tag{A.17}$$

where $\chi$ is again the magnetic susceptibility and $N$ is the demagnetization coefficient, and a some algebraic manipulations, it is possible to identify the second term in (A.16) to be equal to

$$-\frac{\partial E}{\partial e}\ \frac{3(1-e^2)}{2e}. \tag{A.18}$$

Furthermore, using the Lagrangian displacement $\xi_3 = L_{33}x_3$, the first term in (A.16) can be rewritten as

$$-3\eta\dot{L}_{33}\frac{4\pi}{3}R_0^3. \tag{A.19}$$

Finally, using the relation [54]

$$\dot{L}_{33} = \frac{2e\dot{e}}{3(1-e^2)}, \tag{A.20}$$

we arrive at

$$4\pi\eta R_0^3\dot{e} + \frac{\partial E}{\partial e}\left(\frac{3(1-e^2)}{2e}\right)^2 = 0. \tag{A.21}$$

Rewriting this equation as well as the energy of the droplet in terms of an experimentally more convenient parameter – the axis ratio $a/b = 1/\sqrt{1-e^2}$ (we will further denote droplet energy by $\tilde{E}$ and the axis ratio by $e$), allows us to recognize the capillary relaxation time $\tau_c = \eta R_0/\gamma$ in the dynamical equation

$$\frac{d}{dt}\left(\frac{a}{b}\right) = -\frac{1}{\tau_c}\,\frac{9(1-e^2)^{1/2}}{8e}\,\frac{\partial \tilde{E}}{\partial e}. \tag{A.22}$$

Calculation of the series expansion of $\frac{\partial \tilde{E}}{\partial e}$ at either $e_c$ or $H_c$ gives relations of the constants $A$ or $B$ accordingly. The $D$ constant can be easily found after integrating (A.22) and reproducing (4.5) for small $t$:

$$\left(\frac{a}{b}\right) - \left(\frac{a}{b}\right)_c = -\frac{A}{2D}\,\frac{t}{\tau_c}\left(\frac{H^2}{H_c^2} - 1\right). \tag{A.23}$$

The constants determined using this approach yield (4.3.2):

$$A = \frac{8\pi}{3}\,Bm_c\,\frac{6e_c + (e_c^2-3)\log\left[\frac{1+e_c}{1-e_c}\right]}{2e_c^4}, \quad B = -\frac{1}{2}\frac{\partial^3 \tilde{E}}{\partial e^3}\frac{(1-e_c^2)^3}{e_c^2}, \quad D = \frac{8e_c}{9(1-e_c^2)^{1/2}}.$$

# Appendix B

# Bibliography

[1] S. Chandrasekhar, Ellipsoidal Figures of Equilibrium, Yale University Press, Dover, 1969.

[2] G. Taylor, Disintegration of water drops in an electric field, Proceedings of the Royal Society of London. Series A. Mathematical and Physical Sciences 280 (1382) (1964) 383–397. `doi:10.1098/rspa.1964.0151`.
URL `https://royalsocietypublishing.org/doi/10.1098/rspa.1964.0151`

[3] R. Rosensweig, Ferrohydrodynamics, Dover Books on Physics, Dover Publications, 1985.
URL `https://books.google.fr/books?id=ng_DAgAAQBAJ`

[4] V. Drozdova, T. Skrobotova, V. Chekanov, Experimental study of the hydrostatics characterizing the interphase boundary in a ferrofluid, Magnetohydrodynamics 15 (1979) 12–14.

[5] J. Bacri, D. Salin, Instability of ferrofluid magnetic drops under magnetic field, Journal de Physique Lettres 43 (17) (1982) 649–654. `doi:10.1051/jphyslet:019820043017064900`.

URL http://www.edpsciences.org/10.1051/jphyslet:019820043017064900

[6] V. G. Bashtovoi, S. G. Pogirnitskaya, A. G. Reks, Determination of the shape of a free drop of magnetic fluid in a uniform magnetic field, Magnetohydrodynamics (Engl. Transl.); (United States) 23:3.
URL https://www.osti.gov/biblio/6426307

[7] J.-C. Bacri, A. O. Cebers, R. Perzynski, Behavior of a magnetic fluid microdrop in a rotating magnetic field, Physical Review Letters 72 (17) (1994) 2705–2708. doi:10.1103/PhysRevLett.72.2705.
URL https://link.aps.org/doi/10.1103/PhysRevLett.72.2705

[8] K. I. Morozov, A. V. Lebedev, Bifurcations of the shape of a magnetic fluid droplet in a rotating magnetic field, Journal of Experimental and Theoretical Physics 91 (5) (2000) 1029–1032. doi:10.1134/1.1334993.
URL http://link.springer.com/10.1134/1.1334993

[9] A. Cebers, M. Mayorov, Structures of interface a bubble and magnetic fluid in a field, Magnetohydrodynamics 16 (1980) 231–235.

[10] A. O. Tsebers, M. M. Maiorov, Magnetostatic instabilities in plane layers of magnetizable liquids, Magnetohydrodynamics 16 (1) (1980) 21–28.

[11] C. Rigoni, G. Beaune, B. Harnist, F. Sohrabi, J. V. I. Timonen, Ferrofluidic aqueous two-phase system with ultralow interfacial tension and micro-pattern formation, Communications Materials 3 (1) (2022) 26. doi:10.1038/s43246-022-00249-z.
URL https://www.nature.com/articles/s43246-022-00249-z

[12] J.-C. Bacri, D. Salin, Bistability of ferrofluid magnetic drops under magnetic field, 39 (1) 48–50. `doi:10.1016/0304-8853(83)90395-5`.
URL `https://linkinghub.elsevier.com/retrieve/pii/0304885383903955`

[13] A. Cebers, Virial method of investigation of statics and dynamics of drops of magnetizable liquids, Magnetohydrodynamics (Engl. Transl.); (United States) 21.

[14] S. Afkhami, A. J. Tyler, Y. Renardy, M. Renardy, T. G. St. Pierre, R. C. Woodward, J. S. Riffle, Deformation of a hydrophobic ferrofluid droplet suspended in a viscous medium under uniform magnetic fields, Journal of Fluid Mechanics 663 (2010) 358–384. `doi:10.1017/S0022112010003551`.
URL `https://www.cambridge.org/core/product/identifier/S0022112010003551/type/journal_article`

[15] J.-C. Bacri, D. Salin, Dynamics of the shape transition of a magnetic ferrofluid drop, Journal de Physique Lettres 44 (11) (1983) 415–420. `doi:10.1051/jphyslet:019830044011041500`.
URL `http://www.edpsciences.org/10.1051/jphyslet:019830044011041500`

[16] J. V. I. Timonen, M. Latikka, L. Leibler, R. H. A. Ras, O. Ikkala, Switchable Static and Dynamic Self-Assembly of Magnetic Droplets on Superhydrophobic Surfaces, Science 341 (6143) (2013) 253–257. `doi:10.1126/science.1233775`.
URL `https://www.science.org/doi/10.1126/science.1233775`

[17] F. Serwane, A. Mongera, P. Rowghanian, D. A. Kealhofer, A. A. Lucio, Z. M. Hockenbery, O. Campàs, In vivo quantification of spatially varying mechanical properties in developing tissues, Nature Methods 14 (2) (2017) 181–186. `doi:`

10.1038/nmeth.4101.
URL http://www.nature.com/articles/nmeth.4101

[18] R. Zhao, X. Dou, D. Zhang, J. Huang, Numerical study of the magnetohydrodynamic flow instability and its effect on energy conversion in the annular linear induction pump, Physics of Fluids 33 (6) (2021) 067125. doi:10.1063/5.0052564.
URL https://aip.scitation.org/doi/10.1063/5.0052564

[19] S. Zhang, J. Zhou, C. Shao, Numerical investigation on yielding phenomena of magnetorheological fluid flowing through microchannel governed by transverse magnetic field, Physics of Fluids 31 (2) (2019) 022005. doi:10.1063/1.5079624.
URL http://aip.scitation.org/doi/10.1063/1.5079624

[20] E. Al-Hetlani, M. O. Amin, Continuous magnetic droplets and microfluidics: generation, manipulation, synthesis and detection, Microchimica Acta 186 (2) (2019) 55. doi:10.1007/s00604-018-3118-6.
URL http://link.springer.com/10.1007/s00604-018-3118-6

[21] Y. S. Kim, Y. H. Kim, Application of ferro-cobalt magnetic fluid for oil sealing, Journal of Magnetism and Magnetic Materials 267 (1) (2003) 105–110.

[22] P. Das, M. Colombo, D. Prosperi, Recent advances in magnetic fluid hyperthermia for cancer therapy, Colloids and Surfaces B: Biointerfaces 174 (2019) 42–55.

[23] X. Fan, M. Sun, L. Sun, H. Xie, Ferrofluid Droplets as Liquid Microrobots with Multiple Deformabilities, Advanced Functional Materials 30 (24) (2020) 2000138. doi:10.1002/adfm.202000138.
URL https://onlinelibrary.wiley.com/doi/10.1002/adfm.202000138

[24] X. Fan, X. Dong, A. C. Karacakol, H. Xie, M. Sitti, Reconfigurable multifunctional ferrofluid droplet robots, Proceedings of the National Academy of Sciences 117 (45) (2020) 27916–27926. `doi:10.1073/pnas.2016388117`.
URL `http://www.pnas.org/lookup/doi/10.1073/pnas.2016388117`

[25] R. Kay, C. Katrycz, E. J. Heimlich, B. D. Hatton, Programmable droplets: Leveraging digitally-responsive flow fields to actively tune liquid morphologies, PLoS ONE 17.

[26] C. Pozrikidis, A practical guide to boundary element methods with the software library BEMLIB, Chapman & Hall/CRC, 2002.

[27] C. Pozrikidis, Boundary Integral and Singularity Methods for Linearized Viscous Flow, Cambridge University Press, Cambridge, 1992. `doi:10.1017/CBO9780511624124`.
URL `http://ebooks.cambridge.org/ref/id/CBO9780511624124`

[28] R. M. Oliveira, J. A. Miranda, Fully nonlinear simulations of ferrofluid patterns in a radial magnetic field, Phys. Rev. Fluids 5 (2020) 124003. `doi:10.1103/PhysRevFluids.5.124003`.
URL `https://link.aps.org/doi/10.1103/PhysRevFluids.5.124003`

[29] J. D. Sherwood, Breakup of fluid droplets in electric and magnetic fields, Journal of Fluid Mechanics 188 (1988) 133–146. `doi:10.1017/S0022112088000667`.
URL `https://www.cambridge.org/core/product/identifier/S0022112088000667/type/journal_article`

[30] H. A. Stone, J. R. Lister, M. P. Brenner, Drops with conical ends in electric and magnetic fields, Proceedings of the Royal Society of London. Series A: Mathematical, Physical and Engineering Sciences 455 (1981) (1999) 329–347.

`doi:10.1098/rspa.1999.0316`.
URL `https://royalsocietypublishing.org/doi/10.1098/rspa.1999.0316`

[31] O. Lavrova, G. Matthies, T. Mitkova, V. Polevikov, L. Tobiska, Numerical treatment of free surface problems in ferrohydrodynamics, Journal of Physics: Condensed Matter 18 (38) (2006) S2657–S2669. `doi:10.1088/0953-8984/18/38/S09`.
URL `https://iopscience.iop.org/article/10.1088/0953-8984/18/38/S09`

[32] Í. M. Coutinho, J. A. Miranda, Peak instability in an elastic interface ferrofluid, Physics of Fluids 32 (5) (2020) 052104. `doi:10.1063/5.0007381`.
URL `https://doi.org/10.1063/5.0007381`

[33] I. Drikis, J.-C. Bacri, A. Cebers, Labyrinthine pattern formation in disordered system of the magnetic fluid drops: Numerical simulation, Magnetohydrodynamics 35 (1999) 157–169.

[34] A. Z. Zinchenko, M. A. Rother, R. H. Davis, A novel boundary-integral algorithm for viscous interaction of deformable drops, Physics of Fluids 9 (6) (1997) 1493–1511. `doi:10.1063/1.869275`.
URL `http://aip.scitation.org/doi/10.1063/1.869275`

[35] A. Z. Zinchenko, R. H. Davis, Emulsion flow through a packed bed with multiple drop breakup, Journal of Fluid Mechanics 725 (2013) 611–663. `doi:10.1017/jfm.2013.197`.
URL `https://www.cambridge.org/core/product/identifier/S0022112013001973/type/journal_article`

[36] V. Cristini, J. Bławzdziewicz, M. Loewenberg, An Adaptive Mesh Algorithm for Evolving Surfaces: Simulations of Drop Breakup and Coalescence, Journal of

Computational Physics 168 (2) (2001) 445–463. `doi:10.1006/jcph.2001.6713`.
URL `https://linkinghub.elsevier.com/retrieve/pii/S0021999101967130`

[37] X. Ni, B. Zhu, B. Wang, B. Chen, A level-set method for magnetic substance simulation, ACM Transactions on Graphics 39 (4). `doi:10.1145/3386569.3392445`.
URL `https://doi.org/10.1145/3386569.3392445`

[38] W. C. Jesus, A. M. Roma, H. D. Ceniceros, Deformation of a sheared magnetic droplet in a viscous fluid, Commun. Comput. Phys 24 (2018) 332–355.

[39] C. S. Peskin, Flow patterns around heart valves: A numerical method, Journal of Computational Physics 10 (2) (1972) 252–271. `doi:https://doi.org/10.1016/0021-9991(72)90065-4`.
URL `https://www.sciencedirect.com/science/article/pii/0021999172900654`

[40] X. Li, Z.-Q. Dong, P. Yu, X.-D. Niu, L.-P. Wang, D.-C. Li, H. Yamaguchi, Numerical investigation of magnetic multiphase flows by the fractional-step-based multiphase lattice Boltzmann method, Physics of Fluids 32 (8) (2020) 083309. `doi:10.1063/5.0020903`.
URL `http://aip.scitation.org/doi/10.1063/5.0020903`

[41] S. Afkhami, Y. Renardy, Ferrofluids and magnetically guided superparamagnetic particles in flows: a review of simulations and modeling, Journal of Engineering Mathematics 107 (1) (2017) 231–251. `doi:10.1007/s10665-017-9931-9`.
URL `http://link.springer.com/10.1007/s10665-017-9931-9`

[42] D. Das, D. Saintillan, Electrohydrodynamics of viscous drops in strong electric fields: Numerical simulations, Journal of Fluid Mechanics 829 (2017) 127–152, arXiv: 1612.02070. `doi:10.1017/jfm.2017.560`.
URL `http://arxiv.org/abs/1612.02070`

[43] J. Erdmanis, G. Kitenbergs, R. Perzynski, A. Cēbers, Magnetic micro-droplet in rotating field: numerical simulation and comparison with experiment, Journal of Fluid Mechanics 821 (2017) 266–295. `doi:10.1017/jfm.2017.238`.
URL `https://www.cambridge.org/core/product/identifier/S0022112017002385/type/journal_article`

[44] A. Stikuts, R. Perzynski, A. Cēbers, Spontaneous order in ensembles of rotating magnetic droplets, Journal of Magnetism and Magnetic Materials 500 (2020) 166304. `doi:10.1016/j.jmmm.2019.166304`.
URL `https://linkinghub.elsevier.com/retrieve/pii/S030488531932726X`

[45] V. Cristini, Y.-C. Tan, Theory and numerical simulation of droplet dynamics in complex flows—a review, Lab Chip 4 (4) (2004) 257–264. `doi:10.1039/B403226H`.
URL `http://xlink.rsc.org/?DOI=B403226H`

[46] L. Sabat, C. K. Kundu, History of finite element method: A review, in: Recent Developments in Sustainable Infrastructure, Springer Singapore, 2020, pp. 395–404. `doi:10.1007/978-981-15-4577-1_32`.
URL `https://doi.org/10.1007/978-981-15-4577-1_32`

[47] T. Marić, D. B. Kothe, D. Bothe, Unstructured un-split geometrical volume-of-fluid methods – a review, Journal of Computational Physics 420 (2020) 109695.

doi:10.1016/j.jcp.2020.109695.
URL https://doi.org/10.1016/j.jcp.2020.109695

[48] L. Papillon, R. Costello, J. V. Ringwood, Boundary element and integral methods in potential flow theory: a review with a focus on wave energy applications, Journal of Ocean Engineering and Marine Energy 6 (3) (2020) 303–337. doi:10.1007/s40722-020-00175-7.
URL https://doi.org/10.1007/s40722-020-00175-7

[49] Papell Solomon Stephen, Low viscosity magnetic fluid obtained by the colloidal suspension of magnetic particles (Nov. 1965).

[50] J.-C. Bacri, R. Perzynski, D. Salin, Magnetic liquids, Endeavour 12 (2) (1988) 76–83. doi:10.1016/0160-9327(88)90085-3.
URL https://linkinghub.elsevier.com/retrieve/pii/0160932788900853

[51] R. Massart, Preparation of aqueous magnetic liquids in alkaline and acidic media, IEEE Transactions on Magnetics 17 (2) (1981) 1247–1248. doi:10.1109/TMAG.1981.1061188.
URL http://ieeexplore.ieee.org/document/1061188/

[52] E. Dubois, V. Cabuil, F. Boué, R. Perzynski, Structural analogy between aqueous and oily magnetic fluids, The Journal of Chemical Physics 111 (15) (1999) 7147–7160. doi:10.1063/1.480007.
URL https://doi.org/10.1063/1.480007

[53] S. Odenbach (Ed.), Colloidal Magnetic Fluids, Springer Berlin Heidelberg, 2008. doi:10.1007/978-3-540-85387-9.
URL https://doi.org/10.1007/978-3-540-85387-9

[54] E. Blūms, A. O. Cebers, M. M. Maĭorov, Magnetic fluids, Walter de Gruyter, Berlin ; New York, 1997.

[55] J. A. Stratton, Electromagnetic Theory, 1st Edition, McGraw-Hill Companies (New York), 1941, the URL and misc. info are for a re-issue published in 2007 by Wiley-IEEE Press.
URL `http://www.amazon.com/Electromagnetic-Theory-IEEE-Press-Wave/dp/0470131535%3FSubscriptionId%3D13CT5CVB80YFWJEPWS02%26tag%3Dws%26linkCode%3Dxm2%26camp%3D2025%26creative%3D165953%26creativeASIN%3D0470131535`

[56] D. J. Griffiths, Introduction to electrodynamics, Pearson, 2013.

[57] J. D. Jackson, Classical electrodynamics, 3rd Edition, Wiley, New York, NY, 1999.
URL `http://cdsweb.cern.ch/record/490457`

[58] A. Langins, A. P. Stikuts, A. Cēbers, A three-dimensional boundary element method algorithm for simulations of magnetic fluid droplet dynamics, Physics of Fluids 34 (6) (2022) 062105. `doi:10.1063/5.0092532`.
URL `https://aip.scitation.org/doi/10.1063/5.0092532`

[59] I. R. Siqueira, R. B. Rebouças, T. F. Oliveira, F. R. Cunha, A new mesh relaxation approach and automatic time-step control method for boundary integral simulations of a viscous drop, International Journal for Numerical Methods in Fluids 84 (4) (2017) 221–238. `doi:10.1002/fld.4346`.
URL `http://doi.wiley.com/10.1002/fld.4346`

[60] A. V. Knyazev, I. Lashuk, Steepest descent and conjugate gradient methods with variable preconditioning, SIAM Journal on Matrix Analysis and Applications 29 (4) (2008) 1267–1280. `arXiv:https://doi.org/10.1137/060675290`, `doi:10.1137/060675290`.
URL `https://doi.org/10.1137/060675290`

[61] M. Loewenberg, E. J. Hinch, Numerical simulation of a concentrated emulsion in shear flow, Journal of Fluid Mechanics 321 (1996) 395–419. `doi:10.1017/S002211209600777X`.
URL `https://www.cambridge.org/core/product/identifier/S002211209600777X/type/journal_article`

[62] C. Pozrikidis, Interfacial Dynamics for Stokes Flow, Journal of Computational Physics 169 (2) (2001) 250–301. `doi:10.1006/jcph.2000.6582`.
URL `https://linkinghub.elsevier.com/retrieve/pii/S0021999100965823`

[63] A. Z. Zinchenko, M. A. Rother, R. H. Davis, Cusping, capture, and breakup of interacting drops by a curvatureless boundary-integral algorithm, J. Fluid Mech. 391 (1999) 249–292.

[64] S. Kim, S. J. Karrila, Microhydrodynamics: principles and selected applications, Butterworth-Heinemann series in chemical engineering, Butterworth-Heinemann, Boston, 1991.

[65] A. Z. Zinchenko, R. H. Davis, Algorithm for direct numerical simulation of emulsion flow through a granular material 227 (16) 7841–7888. `doi:10.1016/j.jcp.2008.05.004`.
URL `https://linkinghub.elsevier.com/retrieve/pii/S0021999108002660`

[66] Y. Dikansky, A. Cebers, V.P. Shatsky, Magnetic emulsion properties in electric and magnetic fields, Magnetohydrodynamics 26 (1990) 25–30.

[67] J. M. Rallison, A numerical study of the deformation and burst of a viscous drop in general shear flows, Journal of Fluid Mechanics 109 (1981) 465–482. `doi:10.1017/S002211208100116X`.

URL https://www.cambridge.org/core/product/identifier/S002211208100116X/type/journal_article

[68] S. H. Strogatz, Nonlinear Dynamics and Chaos: With Applications to Physics, Biology, Chemistry and Engineering, Westview Press, 2000.

[69] J. W. Strutt, Some general theorems relating to vibrations, Proceedings of the London Mathematical Society 1 (1) (1871) 357–368.

[70] L. D. Landau, E. M. Lifshitz, Mechanics, Third Edition: Volume 1 (Course of Theoretical Physics), 3rd Edition, Butterworth-Heinemann, 1976.
URL http://www.worldcat.org/isbn/0750628960

[71] H. Li, T. C. Halsey, A. Lobkovsky, Singular Shape of a Fluid Drop in an Electric or Magnetic Field, Europhysics Letters (EPL) 27 (8) (1994) 575–580. doi:10.1209/0295-5075/27/8/004.
URL https://iopscience.iop.org/article/10.1209/0295-5075/27/8/004

[72] J. Cīmurs, A. Brasovs, K. Ērglis, Stability analysis of a paramagnetic spheroid in a precessing field, Journal of Magnetism and Magnetic Materials 491 (2019) 165630. doi:10.1016/j.jmmm.2019.165630.
URL https://linkinghub.elsevier.com/retrieve/pii/S0304885318339155

[73] A. Cēbers, M. Ozols, Dynamics of an active magnetic particle in a rotating magnetic field, Physical Review E 73 (2) (2006) 021505. doi:10.1103/PhysRevE.73.021505.
URL https://link.aps.org/doi/10.1103/PhysRevE.73.021505

[74] K. Ērglis, Q. Wen, V. Ose, A. Zeltins, A. Sharipo, P. A. Janmey, A. Cēbers, Dynamics of Magnetotactic Bacteria in a Rotating Magnetic Field, Biophysical

Journal 93 (4) (2007) 1402–1412. `doi:10.1529/biophysj.107.107474`.
URL `https://linkinghub.elsevier.com/retrieve/pii/S000634950771398X`

[75] S. Lācis, A. Cēbers, Magnetic fluid free surface instabilities in high frequency rotating magnetic fields, Brazilian Journal of Physics 25 (1995) 101–111.

[76] A. Sellier, On the computation of the derivatives of potentials on a boundary by using boundary-integral equations, Computer Methods in Applied Mechanics and Engineering 196 (40969) (2006) 489–501. `doi:10.1016/j.cma.2006.05.003`.
URL `https://hal-polytechnique.archives-ouvertes.fr/hal-01023365`